



# Influence of Intermediate Principal Stress on the Strainburst Characteristics of Beishan Granite with Consideration of End Effect

X. G. Zhao<sup>1</sup> · J. Wang<sup>1</sup> · M. Cai<sup>2,3</sup> · G. S. Su<sup>4</sup>

Received: 14 June 2020 / Accepted: 26 May 2021 / Published online: 21 June 2021  
© The Author(s), under exclusive licence to Springer-Verlag GmbH Austria, part of Springer Nature 2021

## Abstract

An experimental study on the strainburst characteristics of Beishan granite under different intermediate principal stress ( $\sigma_2$ ) loading conditions was conducted using a servo-controlled true-triaxial rockburst test machine equipped with an acoustic emission (AE) monitoring system. The primary objective is to investigate the influence of end effect under loading in the  $\sigma_2$  direction on the strainburst behaviors of the rock. Rectangular prism specimens with dimensions of approximately  $200 \times 100 \times 100 \text{ mm}^3$  were prepared and divided into two groups. For the first group, the specimens were in direct contact with platens during loading. For the second group, the specimen's two surfaces loaded by  $\sigma_2$  were daubed with a layer of anti-friction agent to reduce the end friction of the platens. In the test, a loading mode, which kept one specimen surface free and applied loads on another five surfaces of the specimen, was used to simulate the stress state of a rock element on the excavation boundary. A high-speed video camera was used to capture the failure process of the specimens. The experimental results indicate that regardless of the use of the anti-friction agent or not, strainburst characteristics of the specimens depend on the magnitude of  $\sigma_2$ . With increasing  $\sigma_2$ , the degree of violence during rock failure presents an increasing trend and the dynamic failure process of the free specimen surface changes from local rock ejection to full-face burst. However, the  $\sigma_2$ -dependent crack initiation, peak strength, failure mode and energy release characteristics of the lubricated specimens differ significantly from those of the non-lubricated ones. With increasing  $\sigma_2$ , rock strengths increase to a peak value and then decrease, but the peak strength of the lubricated specimen is lower than that of the non-lubricated specimen under a given  $\sigma_2$ . In addition, the peak strength difference between two groups increases as  $\sigma_2$  increases. Meanwhile, large end effect suppresses crack initiation of the specimens, causing crack initiation of the specimens to occur at higher stress levels, leading to higher peak strengths. Moreover, when  $\sigma_2 = 1 \text{ MPa}$ , the failure modes of the non-lubricated and lubricated specimens are similar. When  $\sigma_2$  is greater than  $1 \text{ MPa}$ , the number of the fractures in the surfaces loaded by  $\sigma_2$  for the lubricated specimens is larger than that for the non-lubricated specimens. In addition, the weight and the associated kinetic energy of ejected rock fragments from the lubricated specimen are higher than those from the non-lubricated specimen. The difference of the weight and the kinetic energy of the rock fragments between the non-lubricated and lubricated specimens increases with increasing  $\sigma_2$ .

**Keywords** Strainburst · End effect · Intermediate principal stress · True-triaxial loading · Beishan granite

## Abbreviations

AE	Acoustic emission	URL	Underground research laboratory
FEM	Finite element method	ISRM	International Society for Rock Mechanics and Rock Engineering
DEM	Discrete element method	UCS	Uniaxial compressive strength
EPCA3D	Elasto-Plastic Cellular Automaton		

✉ X. G. Zhao  
xingguang100@126.com

<sup>1</sup> CAEA Innovation Center on Geological Disposal of High Level Radioactive Waste, Beijing Research Institute of Uranium Geology, Beijing 100029, China

<sup>2</sup> Bharti School of Engineering, Laurentian University, Sudbury, ON P3E 2C6, Canada

<sup>3</sup> Key Laboratory of Ministry of Education for Safe Mining of Deep Metal Mines, Northeastern University, Shenyang 110004, China

<sup>4</sup> Key Laboratory of Disaster Prevention and Structural Safety of Ministry of Education, School of Civil and Architecture Engineering, Guangxi University, Nanning 530004, Guangxi, China

SD	Standard deviation
CAEH	Cumulative AE hit

### List of symbols

$\sigma_x$	In-situ stress in $x$ direction
$\sigma_y$	In-situ stress in $y$ direction
$\sigma_z$	In-situ stress in $z$ direction
$K$	Ratio of $\sigma_y$ to $\sigma_x$
$\sigma_1$	Maximum principal stress (MPa)
$\sigma_2$	Intermediate principal stress (MPa)
$\sigma_3$	Minimum principal stress (MPa)
$r$	Radial distance away from the opening boundary
$a$	Opening radius
$\sigma_{ci}$	Crack initiation stress (MPa)
$\sigma_p$	Peak strength (MPa)
$d$	Diameter of standard sieves (mm)
$m$	Mass of an ejected rock fragment (g)
$E_k$	Kinetic energy of an ejected rock fragment (J)
$v$	Speed of an ejected rock fragment (m/s)
$E_{kt}$	Total kinetic energy of the ejected fragments from a rock specimen (J)
$n$	Number of large rock fragments
$m_{li}$	Mass of $i$ th large fragment (g)
$\bar{v}_{li}$	Average speed of several points on the $i$ th large rock fragment (m/s)
$m_c$	Total mass of coarse fragment group (g)
$\bar{v}_c$	Average speed of coarse fragment group (m/s)

## 1 Introduction

As the depth of mining and underground construction increases, stress-induced rock failures near excavation boundaries are inevitable. In some cases, the rock mass fails in an unstable manner, which is normally described as a rockburst (Kaiser et al. 1996). In general, according to occurring mechanisms, rockbursts can be classified into three fundamental types: fault slip bursts, pillar bursts, and strainbursts (Hedley 1992). As the most common rockburst type, strainbursts can be excavation-induced, seismically triggered by a remote seismic event or dynamically loaded by the related stress pulse (Cai and Kaiser 2018). Strainburst poses a significant threat to the safety of workers and stability of underground structures, and its prevention or migration has been one of the most challenging tasks in rock engineering (Kaiser and Cai 2012).

Over the past few decades, considerable effort has been made to address the problem of rockburst. Many experience and lessons have been learned from case histories of rockbursts (Brady and Leighton 1977; Broch and Sørheim 1984; Ortlepp and Stacey 1994; Kaiser et al. 1996, 2000; Feng et al. 2012; Gong et al. 2012; Zhang et al. 2012;

Stacey 2016; Konicek et al. 2018), which contribute to safe construction and operation of excavations at depth. Some theoretical models and numerical methods have been used to study rockbursts or investigate the triggering mechanisms (Wang and Park 2001; Zhu et al. 2010; Adoko et al. 2013; Wang et al. 2015; Manouchehrian and Cai 2016, 2018; Miao et al. 2016). In situ monitoring approaches such as microseismic monitoring have been widely used for monitoring, assessment and warning of rockbursts (Srinivasan et al. 1999; Kaiser 2009; Li et al. 2012; Feng et al. 2015a, 2015b; Ma et al. 2015; Xu et al. 2016). Meanwhile, ground support strategies and techniques have been proposed to control rockburst hazards (Kaiser et al. 1996; Li 2010; Cai and Champaigne 2012; Cai 2013; He et al. 2014; Feng et al. 2017a). Recently, as a major update of the Canadian Rockburst Support Handbook (Kaiser et al. 1996), the Rockburst Support Reference Book has been released (Cai and Kaiser 2018), which aims at providing a comprehensive guidance to creating safe working conditions in burst-prone grounds. However, due to the uncertainties of geological conditions and the complexities of triggering factors in situ, insight into the rockburst mechanism is still limited (Zhao et al. 2014).

Laboratory tests play an important role in understanding rockburst mechanisms, calibration of numerical models, and identification of the stress state where a dynamical failure may be generated (He et al. 2015). Based on conventional uniaxial or triaxial compression test results, many researchers (Cook 1965; Cook et al. 1966; Salamon 1970; Singh 1987; Linkov 1996; Jiang et al. 2015; Miao et al. 2016; Leveille et al. 2017) investigated rockburst mechanisms and evaluated rockburst potential associated mainly with storage and release of strain energy during rock deformation and failure. However, these conventional tests cannot simulate the exact boundary condition for rocks on the excavation boundary, in which an approximate biaxial stress state exists, i.e.,  $\sigma_3 \approx 0$  (the minimum principal stress),  $\sigma_2 \neq 0$  (the intermediate principal stress) and the highest tangential stress (the maximum principal stress,  $\sigma_1$ ) is in the tangential direction of the opening wall, as presented in Fig. 1. In recent years, true-triaxial rockburst tests have been conducted to characterize rock response near the excavation boundaries. For example, He et al. (2007) performed true-triaxial unloading tests using granite specimens and successfully captured the dynamic strainburst process. Using a true-triaxial rockburst test machine equipped with an acoustic emission (AE) monitoring system, He et al. (2010, 2012a) investigated AE frequency-spectra and energy release characteristics of Shuicang limestone and Carrara marble during strainbursts. Zhao et al. (2014) carried out true-triaxial strainburst tests on Beishan granite and discussed the unloading rate-dependent failure behaviors of the rock. Results of true-triaxial unloading tests on Tianhu granite (Zhao and Cai 2015) and Miluo

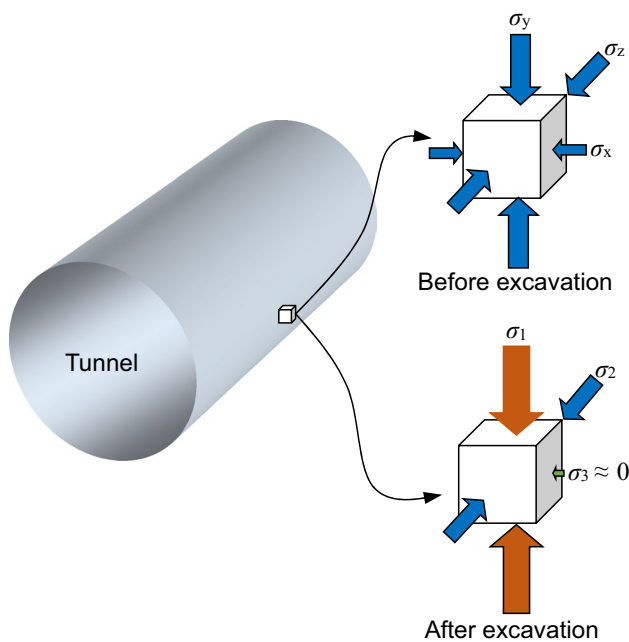


**Fig. 1** Schematic illustration of the stress state of a rock element at the tunnel wall before and after excavation.  $\sigma_x$ ,  $\sigma_y$  and  $\sigma_z$  are in-situ stress components

granite (Li et al. 2018) demonstrated the effect of specimen height-to-width ratio on strainbursts.

Employing a modified less soft rockburst test system (Su et al. 2016), Su et al. (2017a, d) studied the influences of radial stress gradient and thermal treatment temperature on strainbursts of granite under true-triaxial loading conditions. Given that strainbursts can be remotely triggered, Su et al. (2017b, 2018) used the modified true-triaxial rockburst test system to reproduce strainbursts induced by dynamic disturbances applied from different loading directions. While the above-mentioned studies provide meaningful insights into strainbursts induced by different stress paths, experimental investigations on the influence of  $\sigma_2$  on the strainburst characteristics are still limited (Su et al. 2017c; Li et al. 2018). Moreover, in previous true-triaxial strainburst tests, rectangular prism specimens were often in direct contact with steel platens during loading. When  $\sigma_2$  acts on the specimen surfaces, there inevitably exists end friction effect at the interfaces between the specimen and the loading platens. However, the end effect generated from rigid platen loading has not been evaluated regarding the impact of  $\sigma_2$  on rock behaviors in strainburst tests.

It is well known that the strength, deformation and failure characteristics of rocks depend on  $\sigma_2$ . Based on a series of true-triaxial tests on different rock types, some researchers found that for a given  $\sigma_3$ , the strength generally increases with the increase of  $\sigma_2$ , and then decreases when  $\sigma_2$  exceeds a threshold (Mogi 1971, 2007; Haimson and Chang 2000;

Feng et al. 2016; Xu et al. 2017). When the rock specimens failed, the fracture angle presented an increasing trend with the increase of  $\sigma_2$  (Mogi 1972; Haimson and Chang 2000). Based on true-triaxial test data, a few rock strength criteria considering the effect of  $\sigma_2$  were proposed and modified (Wiebols and Cook 1968; Mogi 1971; Haimson and Chang 2000; Yu et al. 2002; Al-Ajmi and Zimmerman 2005; You 2009; Chang and Haimson 2012; Feng et al. 2020). A method to remove the platen-induced  $\sigma_2$  effect on rock strength was proposed by Xu et al. (2020). In addition, true-triaxial cells were used to investigate the process of dilation and the influence of  $\sigma_2$  on the onset of dilation in rocks (Mogi 1977; Takahashi and Koide 1989; Chang and Haimson 2000; Kwasniewski et al. 2003). Similar findings imply that increasing  $\sigma_2$  will restrain the onset of dilation. For hard rocks subjected to true-triaxial loading with one face unloading, Li et al. (2015) observed that the rock failure mode changed from shear to slabbing when  $\sigma_2$  increased to a critical value. To provide a supplement to experimental work, numerical simulations were performed by some to study the influence of  $\sigma_2$  on fracturing and strength of rocks under true-triaxial compression conditions. For example, using a FEM/DEM combined numerical tool, Cai (2008) demonstrated that the generation of in-situ spalling failure (excavation surface parallel fractures) was attributed to rock heterogeneity and the existence of moderate  $\sigma_2$ , while  $\sigma_2$  had limited influence on the strength of the rock near the excavation boundary. He argued that the large percentage increase of rock strength due to  $\sigma_2$  was mainly attributed to the end effect of the testing system. Using the EPCA3D, Pan et al. (2012) found that a moderate  $\sigma_2$  delayed the onset of local failure. Meanwhile, rock heterogeneity and the loading platen-rock interaction were two of the reasons producing the  $\sigma_2$  effect. It should be noted that previous studies focused primarily on the influence of  $\sigma_2$  on static mechanical properties of rocks in true-triaxial tests; strainburst characteristics of rocks subjected to different  $\sigma_2$  loadings have not been fully understood. In particular, there is a lack of information on the influence of end effect at the specimen-loading platen contacts where  $\sigma_2$  is applied on strainbursts.

As the end effect exists in almost every rigid loading test system, different techniques such as brush platen (Brown and Gonano 1974), lubricant (Labuz and Bridell 1993), copper shim combined with lubricant (Haimson and Chang 2000; Lee and Haimson 2011) and steel platen pasted with molybdenum disulfide powder (Yun et al. 2010) were attempted to suppress the friction between the specimen ends and the platens. For instance, using the brush platen as a friction reducer, Brown and Gonano (1974) obtained similar pre-peak stress–strain curves when performing uniaxial compression tests on Wombeyan Marble with various specimen height-to-diameter (slenderness) ratios. Labuz and Bridell (1993) carried out research on the use of a special lubricant

(a mixture of stearic acid and Vaseline) at the rock specimen-platen interfaces. According to the results obtained from double direct shear tests, they demonstrated that the lubricant produced the lowest coefficient of friction compared with Teflon, graphite and molybdenum disulfide. Furthermore, based on stress and strain measurements on different rock cylinders under uniaxial compression, they found that when the lubricant was applied, frictional constraint was significantly reduced and the cylindrical shape was retained during elastic loading. The anti-friction agent has also been used by other researchers to reduce the end effect in uniaxial (Pellegrino et al. 1997) and true-triaxial (Chang and Haimson 2000; Feng et al. 2017b) compression tests.

In the present study, strainburst tests on Beishan granite subjected to different  $\sigma_2$  loadings are conducted using the modified true-triaxial rockburst system (Su et al. 2016). The main objective is to investigate the influence of end effect caused by platens in the  $\sigma_2$  loading direction on strainburst behaviors of the rock. In the following discussion, rock sampling and specimen preparation are introduced first. The test methods and procedures are then described. Subsequently, the effectiveness of the lubricant (Labuz and Bridell 1993) to reduce the end effect is verified from uniaxial compression tests on cylindrical specimens with various slenderness ratios. Finally, crack initiation stress, peak strength, and failure processes of the lubricated and non-lubricated specimens with different  $\sigma_2$  loadings are analyzed, followed by a discussion of the influence of the end effect on ejected rock fragment characteristics and associated kinetic energy during strainbursts.

## 2 Rock Specimen Preparation

Rock sampling was conducted in the Beishan area, located in Gansu Province of northwestern China. The Beishan area is within the Gobi Desert that contains many granite intrusions. A large intact granite block was collected at the Xinchang site in this area, which has been determined as the site for hosting China's first underground research laboratory (URL) for geological disposal of high-level radioactive waste (Wang et al. 2018). The sampling depth ranges between 0.5 and 1.5 m below the ground surface. The sampling location is shown in Fig. 2. The collected rock was gray and had a fine- to medium-grained texture. To evaluate mineralogical composition of the rock quantitatively, three thin sections were prepared and exposed to cross-polarized light to identify the dominant minerals in the rock. The analysis showed that the rock was comprised of approximately 57.7% plagioclase, 6.9% K-feldspar, 29.8% quartz, and 5.6% biotite. A typical thin section photomicrograph of the rock is presented in Fig. 3a.

For the proposed test, a total of 10 intact rectangular prism specimens were prepared from the collected rock block. According to the ISRM suggested method for true-triaxial test (Feng et al. 2019), all six surfaces of the specimens were grinded and polished carefully using a grinding machine to produce flat and smooth end surfaces. Each specimen had dimensions of approximately  $200 \times 100 \times 100 \text{ mm}^3$ , as presented in Fig. 3b. The prepared specimens were equally divided into two groups. For

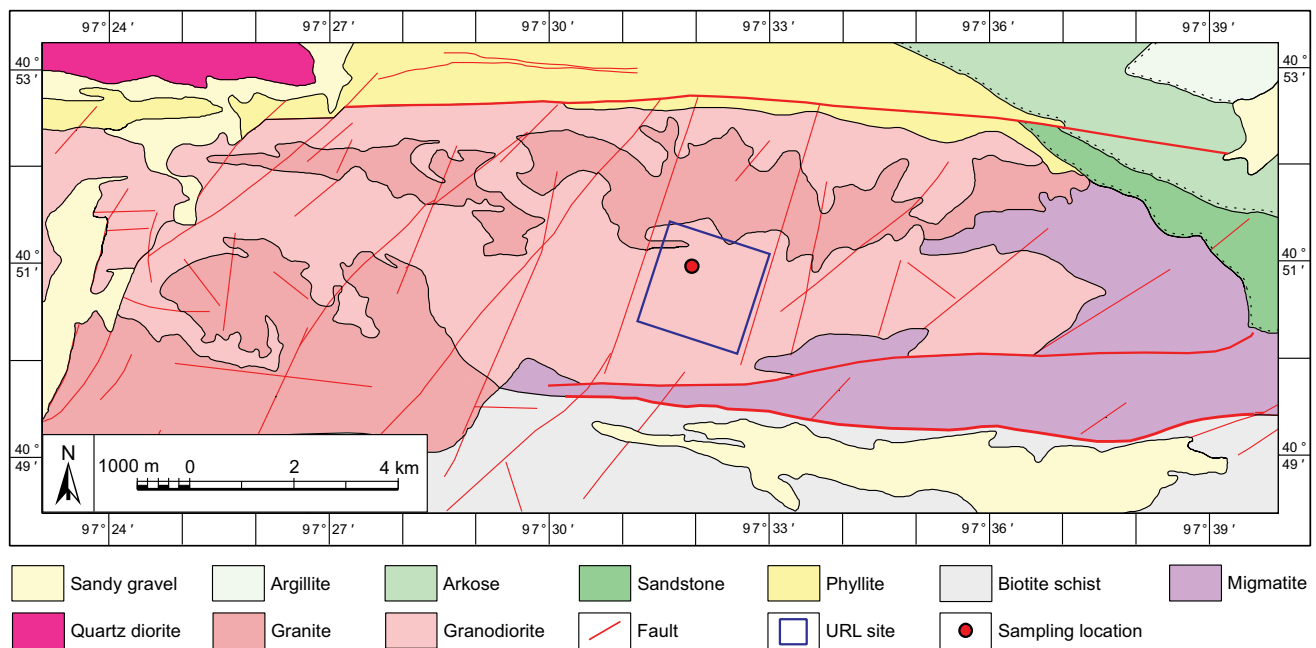


**Fig. 2** A simplified geological map showing the sampling location at the Xinchang site in the Beishan area

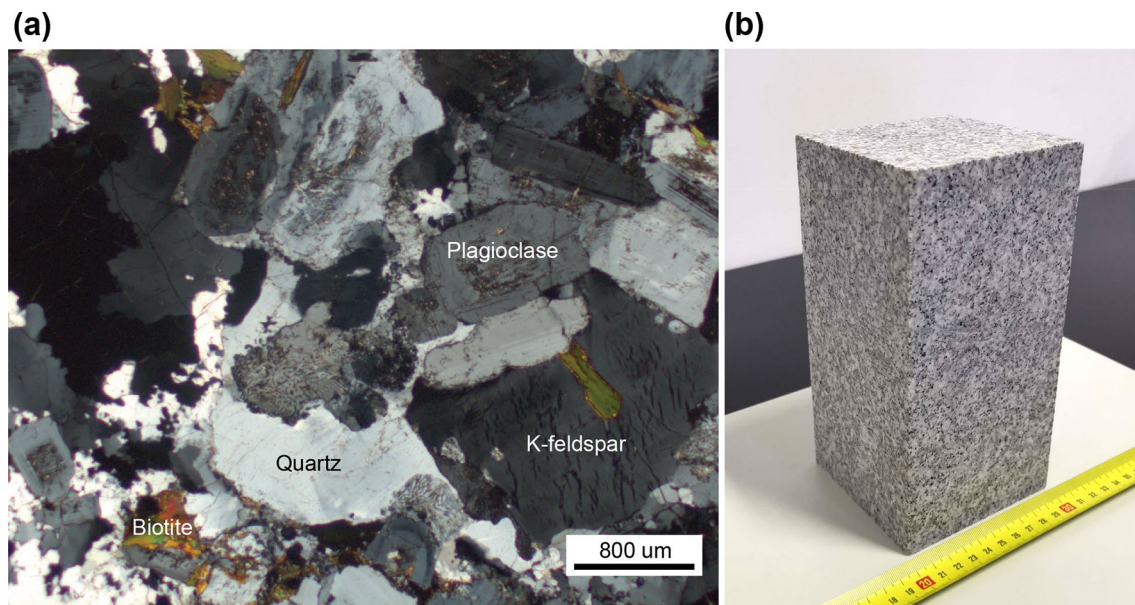


**Fig. 3** A thin section photomicrograph showing the main mineralogical composition of the rock (a), and a prepared rock specimen (b)

the first group, no lubricant was coated at the interfaces between the specimen and the platens. For the second group, the specimen surfaces loaded by  $\sigma_2$  were daubed with a thin layer of anti-friction agent (Labuz and Bridell 1993) to reduce the end effect caused by the platens. To obtain the basic physical and mechanical properties of the rock, tests were conducted using cylindrical samples drilled from the same rock block. The specimens, with a diameter of approximately 50 mm, were prepared in accordance with the specifications recommended by ISRM (ISRM 1978, 1979; Fairhurst and Hudson 1999). The test results show that the rock has a bulk density of 2.63 g/cm<sup>3</sup>. The average uniaxial compressive strength (UCS) and tensile strength are 172 MPa and 9 MPa, respectively, while the average Young's modulus and Poisson's ratio of the rock are 41 GPa and 0.27, respectively.

### 3 Test Methodology

#### 3.1 Test Facility

The modified true-triaxial rockburst test machine (Fig. 4a), which was developed at Guangxi University, China (Su et al. 2016), was used for the test. As a relatively rigid test device compared with that developed by He et al. (2007), this machine can load independently in three principal stress directions with a maximum loading capacity of 5000 kN in the vertical direction and 3000 kN in the two horizontal directions. Compared with the true-triaxial rockburst test system developed by He et al. (2007), the

loading capacity of this machine has been improved significantly. As a result, strainburst tests using hard rock specimens with larger dimensions (200 × 100 × 100 mm<sup>3</sup>, which is about 8 times of the size that can be tested in the system developed by He et al. (2007)) can be performed, reducing the influence of size effect. Meanwhile, stress fluctuations generated from manual control can be removed in the process of loading or unloading due to the use of sophisticated servo-control systems. In addition, a prominent feature of the equipment is that when using a rectangular prism specimen to approximate the rock element in the excavation wall, stress state in this rock element can be characterized in the laboratory by keeping one specimen face free and loading other five faces (Fig. 4b), mimicking the stress state of a small rock unit on the excavation boundary.

This machine is equipped with a high-speed camera and an acoustic emission (AE) monitoring system, which can capture dynamic failure process and record AE signals. An AE sensor (Type Nano30, from American Physical Acoustics Corporation), with an operating frequency range from 150 to 400 kHz, was employed to monitor the cumulative AE hits during loading. AE signals obtained from the AE sensor were amplified by a gain of 40 dB in order to filter out the background noise. The sensor was fixed on the free surface of the specimen, and was in direct contact with the specimen (Fig. 4b). A thin layer of Vaseline was applied to the interface between the specimen and the sensor. The trigger threshold of AE was set to 40 dB for each test, and full waveform data were recorded with a data collection rate of 0.5 MHz.

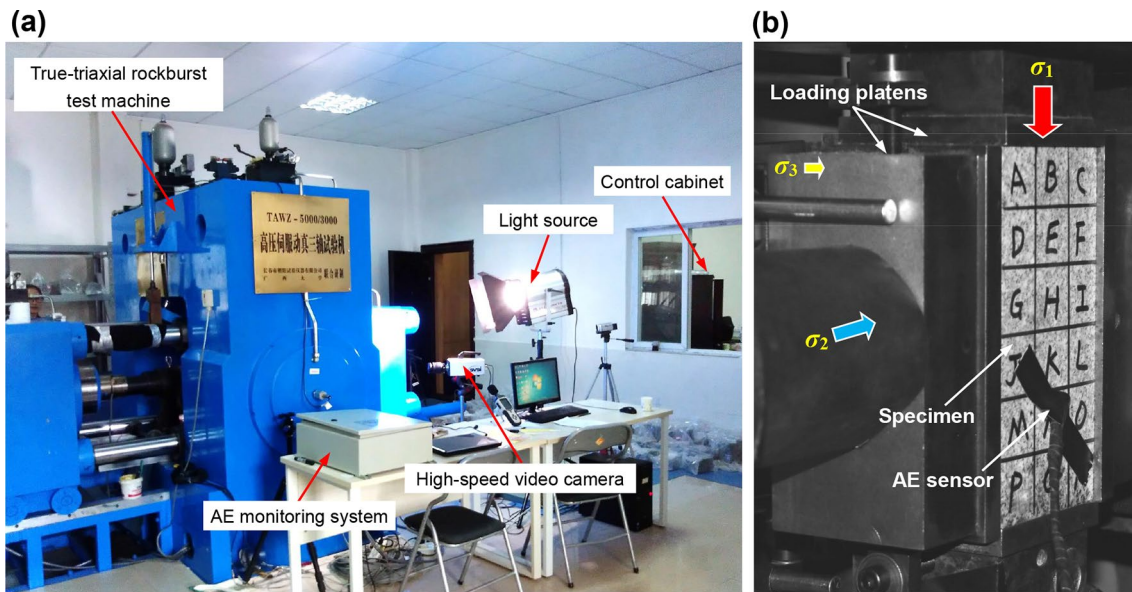


Fig. 4 a The modified true-triaxial rockburst test system (Su et al. 2017b), and b a typical specimen setup

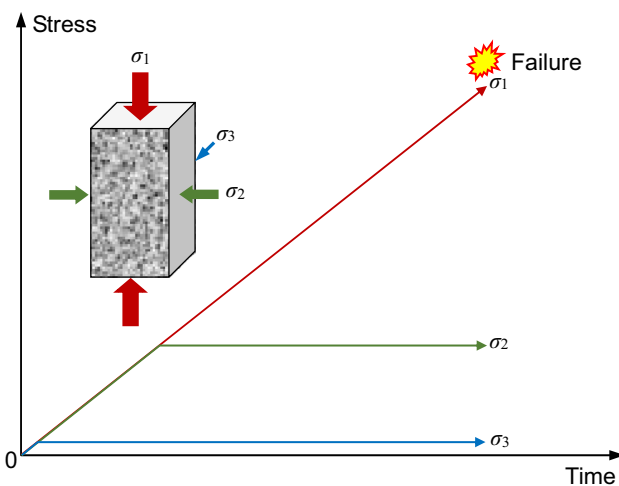


Fig. 5 Schematic illustration of designed stress path in strainburst test

## 3.2 Design of Loading Mode

### 3.2.1 Loading Path

A strainburst can occur right after excavation at the face or can be delayed due to insufficient tangential loading to cause rock failure (Zhao et al. 2014). As the face further advances or when nearby mining occurs, the increase in tangential stress may lead to delayed strainburst. To simulate the behavior of delayed strainbursts in the tests, a true-triaxial loading mode was used in the test. As shown in Fig. 5, for each test, one face of the specimen was kept free before loading. Loads on other five faces were increased at

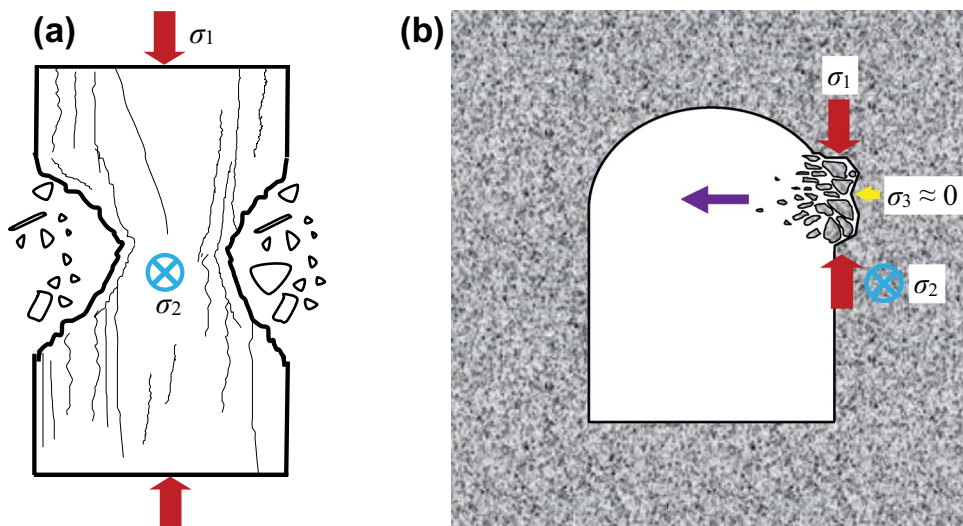
a loading rate of approximately 0.5 MPa/s. When the loads in the  $\sigma_3$  and  $\sigma_2$  directions reached pre-defined stress state, the loads in these two horizontal directions were held constant. Finally, the load in the vertical direction (i.e.,  $\sigma_1$ ) was increased continually to simulate tangential stress concentration until the specimen failed. In this work,  $\sigma_3$  was set to 1 MPa for all tests while different  $\sigma_2$  values (1, 30, 60, 90 and 120 MPa) were adopted.

### 3.2.2 Discussion on Stress State of the Specimen

As mentioned in *Introduction*, an approximate biaxial loading condition of  $\sigma_3 \approx 0$ ,  $\sigma_1 \neq 0$ , and  $\sigma_2 \neq 0$  exists for rocks on the opening walls (Fig. 1). Hence, the biaxial compression test can be used to approximately represent the stress state of a thin rock element on the excavation boundary. However, when conducting a strainburst test on a specimen under biaxial compression, rock fragments may be ejected from the two opposite free surfaces when the specimen fails (Fig. 6a). This behavior is not in agreement with field observations, in which failed rocks are ejected only from the free excavation surface (Fig. 6b). In order to reproduce strainbursts in our test, a relatively small stress (i.e.,  $\sigma_3 = 1$  MPa) was applied on the opposite side of the free surface of the specimen. This loading mode not only makes rock fragments ejected only from the free surface of the specimen, but also makes it possible to study the influence of  $\sigma_2$  on strainbursts when increasing  $\sigma_1$  and while keeping  $\sigma_2$  and  $\sigma_3$  unchanged.

Near the excavation boundary,  $\sigma_3$  is low and depends on in-situ stress conditions and excavation geometry. In the simplest case, a circular opening with a radius of  $a$  is assumed

**Fig. 6** Comparison of laboratory and in-situ observations on dynamic rock failure induced by biaxial compression. **a** Ejection of rock fragments from two opposite free surfaces of the specimen, and **b** ejection of rocks from the tunnel wall

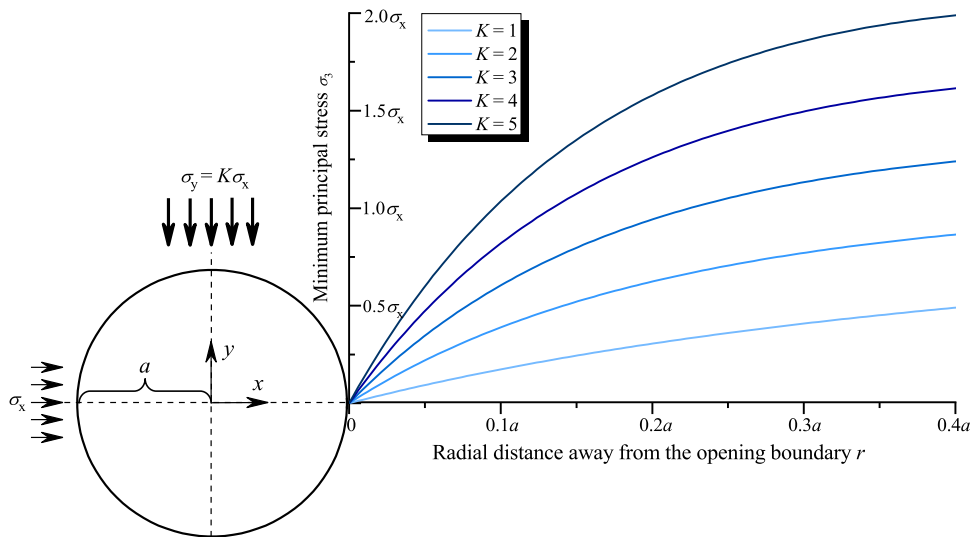


to be excavated in a homogenous, isotropic, and elastic rock mass. According to the Kirsch's solution, the distribution of  $\sigma_3$  near the opening boundary is shown in Fig. 7. It is seen that regardless of  $K$  (the ratio of vertical stress  $\sigma_y$  to horizontal stress  $\sigma_x$ ),  $\sigma_3$  increases nonlinearly with increasing radial distance away from the opening boundary ( $r$ ). In addition, under a constant  $r$ , the larger  $K$  is, the larger  $\sigma_3$  is. For example, when excavating a 10 m diameter tunnel subjected to a constant  $\sigma_x$  of 10 MPa and various  $K$  values ranging from 1 to 5,  $\sigma_3$  at a point with  $r = 10$  cm increases linearly from 0.4 to 2.6 MPa with increasing  $K$ . In our test,  $\sigma_3 = 1$  MPa was adopted by a trial-and-error process. If a relatively large  $\sigma_3$  was used, the shear stresses resulting from end friction on the non-free specimen surfaces would be very high. The stresses cannot simulate the approximate biaxial loading condition reasonably. On the contrary, if a very small  $\sigma_3$  was used, excessive expansion deformation of the specimen in

the direction opposite to the normal direction of the free surface would occur when increasing  $\sigma_1$ , which is inconsistent with the field situation where the rock mainly dilates towards to opening, i.e., in the normal direction of the free surface. For this reason, we designed the strainburst test, which was featured by keeping one specimen face free, applying a constant small  $\sigma_3$  of 1 MPa on the opposite side of the free face, and loading other four faces. This is a reasonable representation of the stress state of rock units on the excavation walls.

It should be pointed out that the stress loading condition adopted in this study is different from the traditional true-triaxial loading condition where an equal amount of  $\sigma_3$  is applied to two surfaces of a specimen. In our case, when  $\sigma_3$  is applied on the opposite side of the free specimen surface, shear stresses appear between the specimen surfaces and the loading platens, as shown in Fig. 8. The applied vertical stress in the  $z$ -direction and horizontal

**Fig. 7** Distributions of  $\sigma_3$  near a circular opening boundary under different ratios of vertical stress to horizontal stress



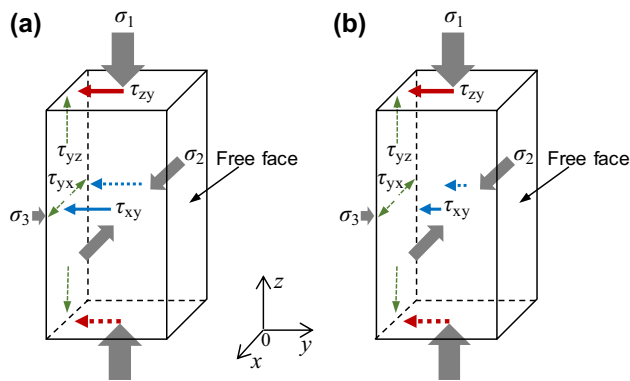


**Fig. 8** Schematic illustration of the stress state of the rock specimen in the one-face-free true-triaxial tests: **a** Non-lubricated specimen, and **b** lubricated specimen.  $\tau_{xy}$ ,  $\tau_{yx}$ ,  $\tau_{xz}$ , and  $\tau_{zx}$  are shear stresses on different specimen surfaces

stress in the  $y$ -direction (Fig. 8) in the test are strictly not the principal stresses, but the tangential and radial stress for a rock unit on the tunnel wall. Given that the applied  $\sigma_3$  is small (1 MPa), the load caused by it applied to one surface is balanced by the friction between the specimen and the platens for  $\sigma_1$  and  $\sigma_2$  loadings for non-lubricated specimens (Fig. 8a). For lubricated specimens, it is balanced mostly by the friction between the specimen and the platens for  $\sigma_1$  loading when the end friction on specimen surfaces loaded by  $\sigma_2$  is reduced significantly (Fig. 8b). In addition, the applied  $\sigma_3$  is very small compared with the failure stress of the tested rock. The magnitude and orientation of  $\sigma_1$  are not significantly influenced by the applied  $\sigma_3$ . Hence, the applied  $\sigma_1$  and  $\sigma_3$  in the test are approximately regarded as the principal stresses. Note that  $\sigma_2$  is not affected by the applied  $\sigma_3$ . Alternatively, we can call  $\sigma_1$ ,  $\sigma_2$ , and  $\sigma_3$  as tangential stress, axial stress, and radial stress, respectively.

In all laboratory loading tests, increasing  $\sigma_1$  will cause the specimen to expand. Hence, the end effect in surfaces loaded by  $\sigma_1$  cannot be eliminated. In order to reduce the influence of the end effect in the  $\sigma_1$  direction on rock strength, we used rectangular specimens with a ratio of height-to-width ratio of 2.0. It should be mentioned that the end effect on rock strength and deformation always exists in triaxial test results (Xu et al. 2017, 2020). The mechanical response of the tested specimens may be different from those without end effect in the  $\sigma_1$  direction. However, the primary objective of this paper is to investigate the influence of end effect under loading in the  $\sigma_2$  direction on the strainburst behaviors of the rock. Under the same conditions, the differences of failure process, crack initiation stress, peak strength, ejected rock fragment characteristics, and kinetic energy of the ejected fragments

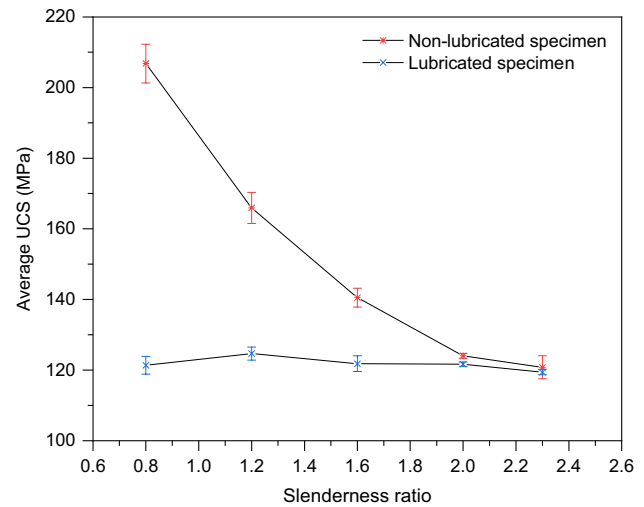


**Fig. 9** Influence of end lubrication on UCS of the specimens with different slenderness ratios. Error bars indicate the standard deviation of UCS

between lubricated and non-lubricated specimens are main concerns.

#### 4 Verification of the Performance of the Anti-friction Agent

Before the strainburst tests were performed, uniaxial compression tests on cylindrical specimens were conducted to verify the performance of the anti-friction agent on reducing the end effect caused by platens. The anti-friction agent was prepared by placing stearic acid crystals and Vaseline at a weight ratio of 1:1 in an oven and slowly heating to 70 °C, and then cooling in cold water (Labuz and Bridell 1993). It should be mentioned that due to limited number of specimens for the strainburst tests, the rock used for uniaxial compression tests was collected from the Jijicao site in the Beishan area (Zhao et al. 2015a). Altogether 33 cylindrical specimens, 50 mm in diameter with different specimen slenderness (length-to-diameter) ratios ranging from 0.8 to 2.3, were prepared from a large granitic rock block. To investigate the difference of UCSs between the non-lubricated and lubricated specimens, these specimens were divided into two groups. For this test, three or four specimens for each specimen size were prepared in each group.

The average UCS values of the non-lubricated and lubricated specimens with five different slenderness ratios are presented in Fig. 9. A statistical analysis shows that for each data point in Fig. 9, the standard deviation (SD) is less than 5.5 MPa, which indicates that for each specimen group, the UCS values between the specimens with the same slenderness ratio are very consistent. For the non-lubricated



specimens, the average UCS decreases remarkably with increasing specimen slenderness ratio, but the value tends to be constant at specimen slenderness ratios between 2.0 and 2.3. This reflects that the friction effect on the platens starts to weaken when the specimen slenderness ratio is larger than 2.0. The average UCS value of the non-lubricated specimens with a slenderness ratio of 0.8 is 67% higher than that of specimens with a slenderness ratio of 2.0. As specified in the ISRM suggested method for determining the complete stress–strain curve for intact rock in uniaxial compression (Fairhurst and Hudson 1999), cylindrical rock specimens are required to have a height-to-diameter ratio of between 2.0 and 3.0 for minimizing the end effects. It is seen from Fig. 9 that when the anti-friction agent was applied to the specimen end surfaces, the average UCS values are almost identical for the specimens with different slenderness ratios, revealing that the friction constraint between the specimen ends and platens has been greatly reduced. Hence, in our strainburst tests, the end effect under loading in the short-axis direction related to  $\sigma_2$  could be suppressed effectively when using the anti-friction agent.

## 5 Strainburst Test Results

### 5.1 Influence of End Effect on Crack Initiation Stress and Peak Strength

Strainburst tests on all 10 specimens were conducted successfully. The crack initiation stress ( $\sigma_{ci}$ ) and peak strength ( $\sigma_p$ ) of the specimens were determined.  $\sigma_{ci}$  is one of the important stress thresholds during the deformation process of rocks under compression. It can be used to estimate rock strength parameters such as tensile strength and Hoek–Brown strength parameter  $m_i$  (Cai 2009, 2010).  $\sigma_{ci}$  can be defined by the onset of stable crack growth or dilation (Brace et al. 1966). Over the last 50 years, various methods based on strain and AE measurements have been proposed to determine  $\sigma_{ci}$  in compression tests (Brace et al. 1966; Lajtai 1974; Stacey 1981; Martin and Chandler 1994; Eberhardt et al. 1999; Diederichs 2007; Nicksiar and Martin 2012; Zhao et al. 2013, 2015b). Among these methods, the cumulative AE hit (CAEH) method, which was developed by (Zhao et al. 2015b, 2015c), is an AE-based method for objective determination of  $\sigma_{ci}$ . Using 20 granite specimens, Zhao et al. (2015b) compared the crack initiation stress thresholds determined by the CAEH method with those by several strain-based and AE-based methods, and the good agreement between the results by these methods suggested that the CAEH method could be used for accurate determination of crack initiation stress of brittle rocks. Because strain measurement was not conducted in this work, the CAEH method was used to identify  $\sigma_{ci}$  of the specimens using the

recorded relations between  $\sigma_1$  and the cumulative AE hits of the specimens. Taking the non-lubricated specimen under a  $\sigma_2$  of 1 MPa for example (Fig. 10), the interpretation of  $\sigma_{ci}$  is presented as follows:

1. Determination of the upper bound: In the plot of the cumulative AE hits versus  $\sigma_1$  up to the peak strength  $\sigma_p$  (Fig. 10a), a random point at the distinct convex section at the initial loading stage is selected as the initial point. Starting at the selected initial point and finishing at the end point (i.e.,  $\sigma_p$ ) of the AE curve, data points on the curve are connected to the origin at zero stress by straight lines. The slopes of these straight lines are determined. The point that corresponds to the minimum slope of the straight lines is chosen as the upper bound point for establishing  $\sigma_{ci}$  (Fig. 10a).
2. Determination of the lower bound: Fig. 10b shows a zoomed-in region between the initial point and the upper bound established in the previous step. The data points between the initial point and the upper bound point on the AE curve are connected to the upper bound point using straight lines. The corresponding slopes of these straight lines can be again determined (Fig. 10b), and the point that corresponds to the minimum slope is chosen as the lower bound point for establishing  $\sigma_{ci}$ .
3. Identification of  $\sigma_{ci}$ : Fig. 10c presents a zoomed-in region between the upper and lower bounds obtained in the previous two steps. A reference line can be generated by connecting the lower bound to the upper bound points. As shown in Fig. 10c, the difference between the measured cumulative AE hit number and the established reference line, which is called cumulative AE hit difference, can be determined.  $\sigma_1$  that corresponds to the maximum cumulative AE hit difference is assumed to be  $\sigma_{ci}$  (Fig. 10d).

Figure 11 shows variations of  $\sigma_{ci}$  and  $\sigma_p$  of the specimens with  $\sigma_2$ . Compared with  $\sigma_p$ ,  $\sigma_{ci}$  of the specimens is less dependent on  $\sigma_2$ . For the non-lubricated specimens loaded by  $\sigma_2$  ranging from 1 to 90 MPa,  $\sigma_{ci}$  increases with the increase of  $\sigma_2$ , and the increase at  $\sigma_2 = 90$  MPa is 48% higher than that at  $\sigma_2 = 1$  MPa (Fig. 11a). This indicates that the onset of crack growth is significantly delayed with the increase of  $\sigma_2$ , which makes  $\sigma_p$  increase in a large percentage (Fig. 11b). It is also found that when  $\sigma_2$  is less than 90 MPa,  $\sigma_{ci}$  of the non-lubricated specimens is greater than  $\sigma_2$ , indicating that crack initiation occurs during  $\sigma_1$  loading with a constant  $\sigma_2$ . However, when the target  $\sigma_2$  was set to 120 MPa, crack initiation of the non-lubricated specimen occurred in the process of increasing  $\sigma_1$  and  $\sigma_2$ , i.e., cracks initiated in the specimen before the predefined target  $\sigma_2$  (120 MPa) was reached (see the data point on the diagonal line in Fig. 11a). Once crack initiation occurs, further

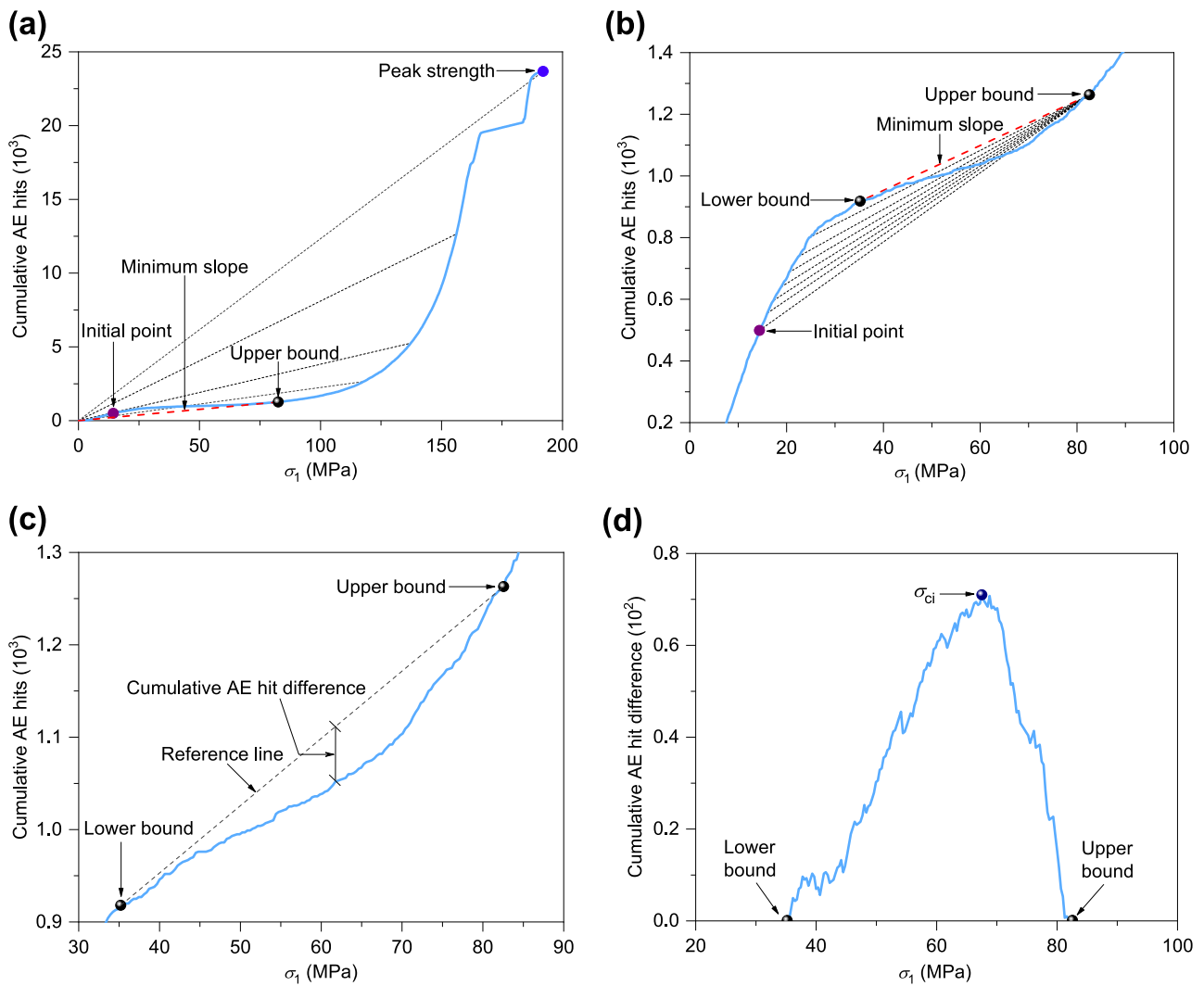


**Fig. 10** The CAEH method (Zhao et al. 2015b) used to determine  $\sigma_{ci}$  of the non-lubricated specimen subjected to a  $\sigma_2$  of 1 MPa. **a** Determination of the upper bound and **b** the lower bound for establishing  $\sigma_{ci}$ , **c** a zoomed-in region of the reference line between the upper and

lower bounds for calculating the cumulative AE hit difference, and **d** identification of  $\sigma_{ci}$  (notice the different scales for the vertical axis in (a) to (c))

synchronous increase of  $\sigma_1$  and  $\sigma_2$  may accelerate crack propagation at a low  $\sigma_3$ , which may lead to the decrease in  $\sigma_p$  (Fig. 11b). In addition,  $\sigma_{ci}$  of the non-lubricated specimen at  $\sigma_2 = 101$  MPa is lower than that of the non-lubricated specimen at  $\sigma_2 = 90$  MPa. This may reflect that if  $\sigma_2$  is enough large, cracks are easier to initiate at a lower  $\sigma_1$ .

When  $\sigma_2 = 1$  MPa,  $\sigma_{ci}$  values of the non-lubricated and lubricated specimens are comparable because of a small end effect. As  $\sigma_2$  increases, the  $\sigma_{ci}$  values of the non-lubricated specimens are higher than those of the lubricated specimens, indicating that the end effect increases with increasing  $\sigma_2$  and suppresses the initiation of cracks in the specimens. In other words, when the end effect is reduced by the anti-friction agent, crack initiation can be induced at a lower stress

level, resulting in a lower peak strength of the specimen. In addition,  $\sigma_{ci}$  values of all the lubricated specimens only range from 71 to 88 MPa, reflecting low sensitivity to variations in  $\sigma_2$ . Note that when  $\sigma_1$  and  $\sigma_2$  were simultaneously increased to be close to 90 MPa, crack initiation occurred for the lubricated specimens (see the two data points on the diagonal line in Fig. 11a), i.e.,  $\sigma_{ci}$  was independent on the predefined target  $\sigma_2$  values (90 and 120 MPa).

It is seen from Fig. 11b that with the increase of  $\sigma_2$ ,  $\sigma_p$  of the specimens increases gradually until a peak value is reached, and then decreases as  $\sigma_2$  further increases. This behavior (i.e.,  $\sigma_2$  effect) was also widely observed in conventional true-triaxial compression tests (Mogi 1971, 2007; Haimson and Chang 2000; Feng et al. 2016; Xu et al. 2017).

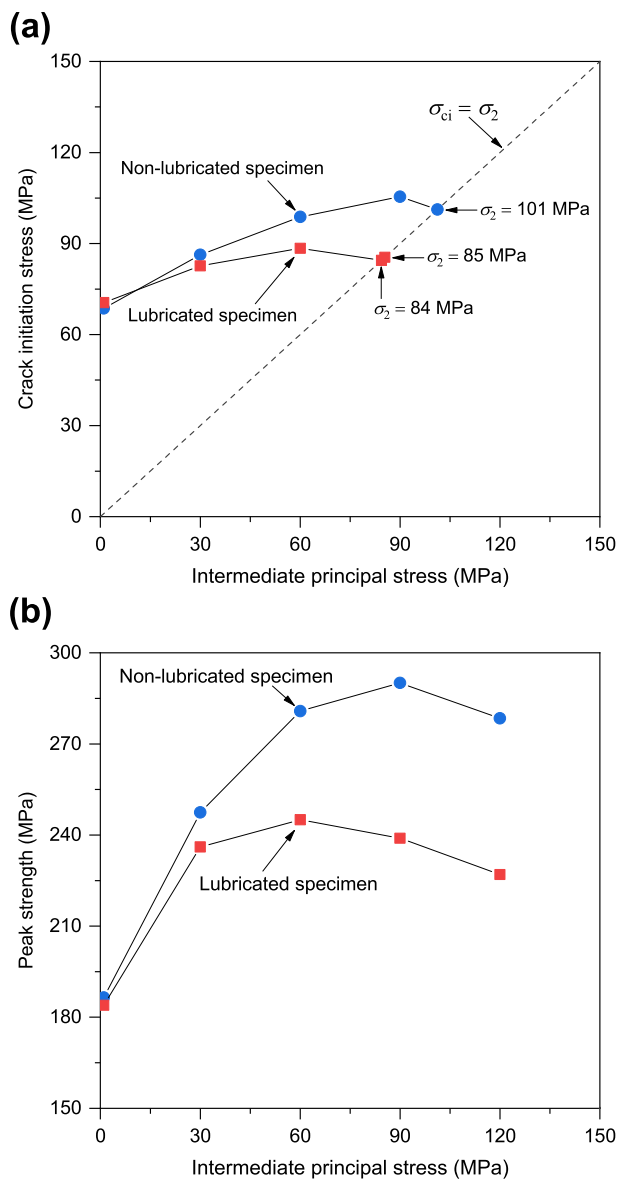


**Fig. 11** Variations of the crack initiation stress and peak strength of the specimens with  $\sigma_2$ . **a** Crack initiation stress and **b** peak strength

However, significant differences exist in  $\sigma_p$  between the non-lubricated and lubricated specimens. At any given  $\sigma_2$ ,  $\sigma_p$  of the non-lubricated specimen is higher than that of the lubricated specimen. Meanwhile, the variation of  $\sigma_2$  has an important influence on the strength difference between the non-lubricated and lubricated specimens. For example, when  $\sigma_2 = 1$  MPa, the strength difference is only 3 MPa. With increasing  $\sigma_2$ , the strength difference increases gradually. When  $\sigma_2 = 120$  MPa, the strength difference reaches 51 MPa. This means that the higher the  $\sigma_2$  is, the higher the end effect caused by the friction on  $\sigma_p$  is. This phenomenon is attributed to the difference of the end effect between the non-lubricated and lubricated specimens. For the non-lubricated

specimens, the observed strength leads to an overestimation of the actual  $\sigma_p$  due to a large end effect, especially when  $\sigma_2$  is larger than 30 MPa. When the anti-friction agent was used, the platen end effect was reduced significantly. Hence, the obtained  $\sigma_p$  is close to the actual strength of the rock, which could be reckoned if the friction coefficients of the lubricated or non-lubricated contact are known (Xu et al. 2020). In addition,  $\sigma_p$  peaks at  $\sigma_2 = 90$  MPa for the non-lubricated specimens while it peaks at  $\sigma_2 = 60$  MPa for the lubricated specimens, indicating that with the increase of  $\sigma_2$ , the end effect causes the appearance of the highest rock strength to be delayed.

Evidence of platen-induced end effect can also be seen in the photographs of the failed specimens after testing (Fig. 12). When  $\sigma_2 = 1$  MPa, the failure mode of the specimens is dominated by splitting, i.e., the orientations of the fractures are approximately parallel to  $\sigma_1$  and  $\sigma_2$ . When  $\sigma_2$  is increased to 30 MPa, splitting failure coupled with a few shear fractures start to appear in the specimen surfaces perpendicular to the direction of  $\sigma_2$ . With  $\sigma_2$  is increased from 60 to 120 MPa, the non-lubricated specimens mainly present shear failure (Fig. 12a). The shear-fracture-dominated failure is an indicator of generation of remarkable end friction effect, which changes the stress condition and hence the final failure mode of the specimens (Cai 2008; Zhao and Cai 2015). However, the lubricated specimens primarily show splitting failure behavior in the  $\sigma_1$ - $\sigma_2$  plane (Fig. 12b). For example, at  $\sigma_2 = 120$  MPa, the specimens were split into many thin rock slabs after the tests, as observed in rocks near the excavation boundaries and demonstrated using 3D FEM/DEM models (Cai 2008). In addition, under the same  $\sigma_2$  loading condition, the number of the fractures in the surfaces loaded by  $\sigma_2$  for the lubricated specimens is more than that for the non-lubricated specimens. This may illustrate that when the end effect is reduced, the cracks in the specimens are easy to grow near excavation boundaries (represented in the tests by having one free surface and a low  $\sigma_3 = 1$  MPa acting on the opposite surface of the specimens). Hence,  $\sigma_p$  of the lubricated specimen is lower than that of non-lubricated specimen under the same  $\sigma_2$ .

### 5.2 Influence of End Effect on Failure Process

The dynamic failure processes of the specimens under different  $\sigma_2$  loading conditions were captured using the high-speed video camera. A series of snapshots for the non-lubricated and lubricated specimens are shown in Figs. 13 and 14, respectively. In general, the strainburst process on the free specimen surface can be characterized by three typical stages, i.e., random ejection of rock particles, local splitting or bending of rock slabs, and violent ejection of rock fragments (Fig. 13a). Similar descriptions on the strainburst processes of rocks in previous true-triaxial unloading or loading

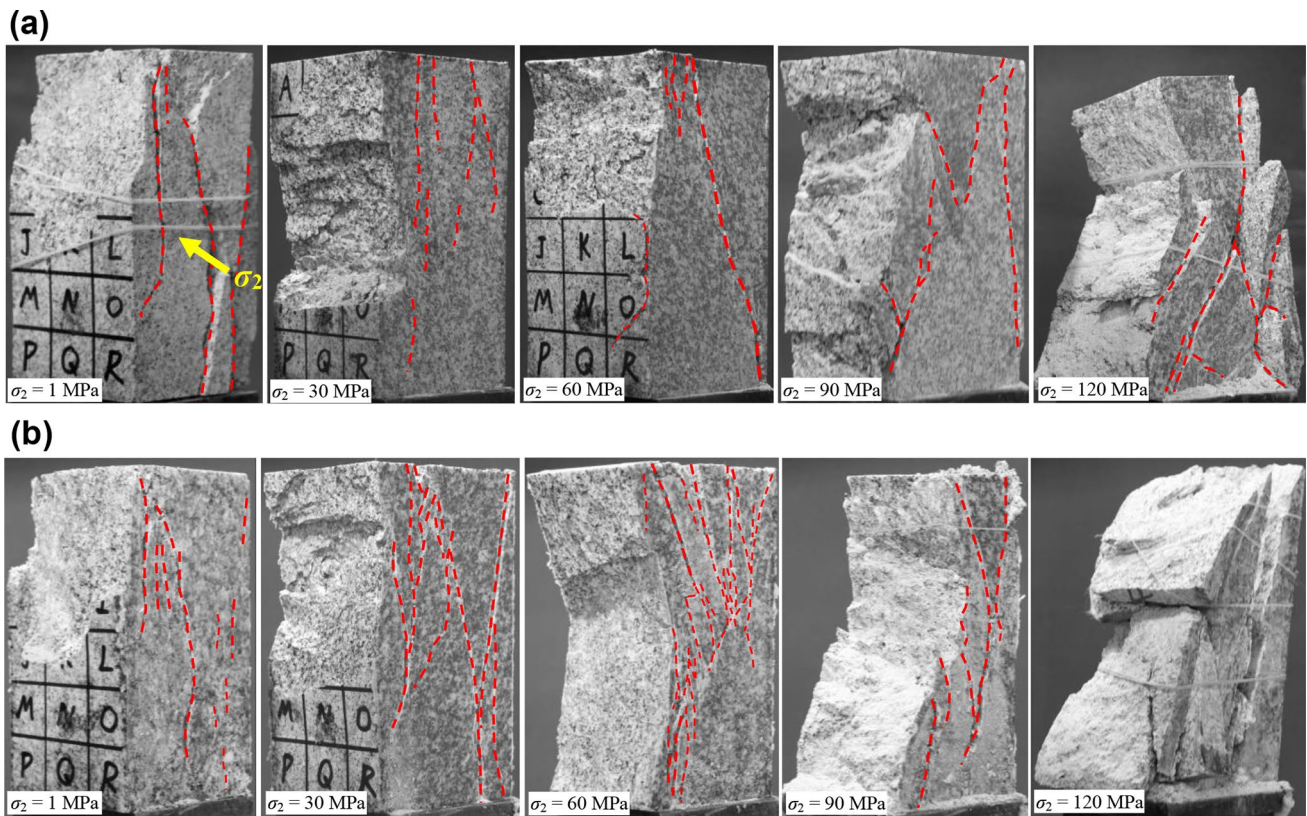


**Fig. 12** Failed specimens after the strainburst tests with different  $\sigma_2$  loadings. **a** Non-lubricated specimens and **b** lubricated specimens. The red dotted lines indicate the observed fracture traces in specimen surfaces perpendicular to  $\sigma_2$

tests can be found in He et al. (2012b), Zhao et al. (2014), and Su et al. (2017d).

Analysis of Figs. 13 and 14 shows that regardless of the use of the anti-friction agent or not, the magnitude of  $\sigma_2$  influences the dynamic failure behaviors of the specimens. A common phenomenon was that strainbursts were more violent for the specimens under higher  $\sigma_2$  loading conditions. For example, for the non-lubricated specimens loaded by  $\sigma_2$  ranging from 1 to 60 MPa, strainbursts occurred on partial regions of the specimens and rock fragments were ejected locally from the failure locations (Fig. 13a–c). Meanwhile, the volumes of the burst pits (i.e., the pits left behind after ejection of rock fragments) for the three specimens were comparable (Fig. 12a), indicating that within this range of  $\sigma_2$ , the volume of rock pieces peeled from the specimens during strainbursts was not sensitive to  $\sigma_2$ . When  $\sigma_2$  was increased to 90 MPa, rock failure was more violent than that for  $\sigma_2$  less than 60 MPa and failure appeared on the full free surface of the specimen (Fig. 13d), leading to the formation of a larger burst pit (Fig. 12a,  $\sigma_2=90$  MPa). With a further increase of  $\sigma_2$  to 120 MPa, an intensive strainburst occurred (Fig. 13e) and the instantaneous eruption of the strainburst caused a collapse of the specimen (Fig. 12a,  $\sigma_2=120$  MPa).

The  $\sigma_2$ -dependent failure processes of the lubricated specimens differ from those of non-lubricated specimens. When  $\sigma_2$  ranged between 1 and 30 MPa, the strainburst process of the lubricated specimens on the free surface was dominated by local ejection of rock fragments (Fig. 14a and b), which was similar to that of non-lubricated specimens (Fig. 13a and b). When  $\sigma_2$  was increased from 30 to 60 MPa, the failure behavior of the lubricated specimen transformed from local rock ejection to full-face burst (Fig. 14c), and the burst pit volume of the lubricated specimens increased (Fig. 12b,  $\sigma_2=60$  MPa). With increasing  $\sigma_2$  from 60 to 90 MPa, the degree of violence during failure of the lubricated specimens increased (Fig. 14d), and the burst pit volume of the specimen increased significantly (Fig. 12b,  $\sigma_2=90$  MPa). When  $\sigma_2=120$  MPa, the lubricated specimen bursted violently. A large amount of rock fragments were ejected at high speeds from the free surface (Fig. 14e), and the specimen was broken into many rock pieces (Fig. 12b,  $\sigma_2=120$  MPa). It is seen from Fig. 13 and 14 that under a  $\sigma_2$  ranging from 30 to 120 MPa, the strainburst intensity of the lubricated specimen is higher than that of the non-lubricated specimen.

Based on the above findings, it can be concluded that dynamic failure behaviors of the specimens under different  $\sigma_2$  conditions depend strongly on the end effect. When

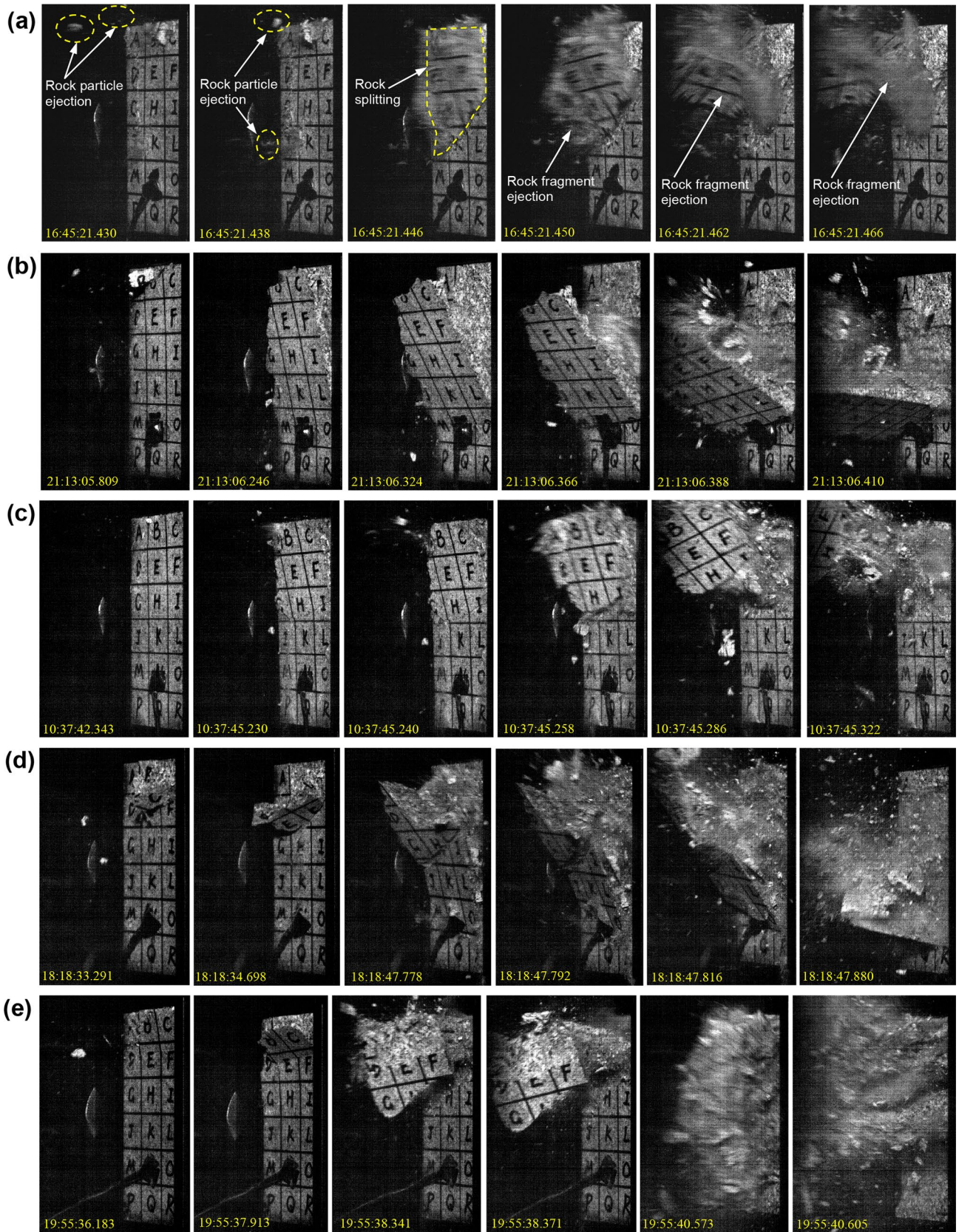


**Fig. 13** Failure processes of the non-lubricated specimens under different  $\sigma_2$  loading conditions: **a** 1 MPa, **b** 30 MPa, **c** 60 MPa, **d** 90 MPa, and **e** 120 MPa. The numbers at the bottom-left corner of the pictures indicate time in h:m:s

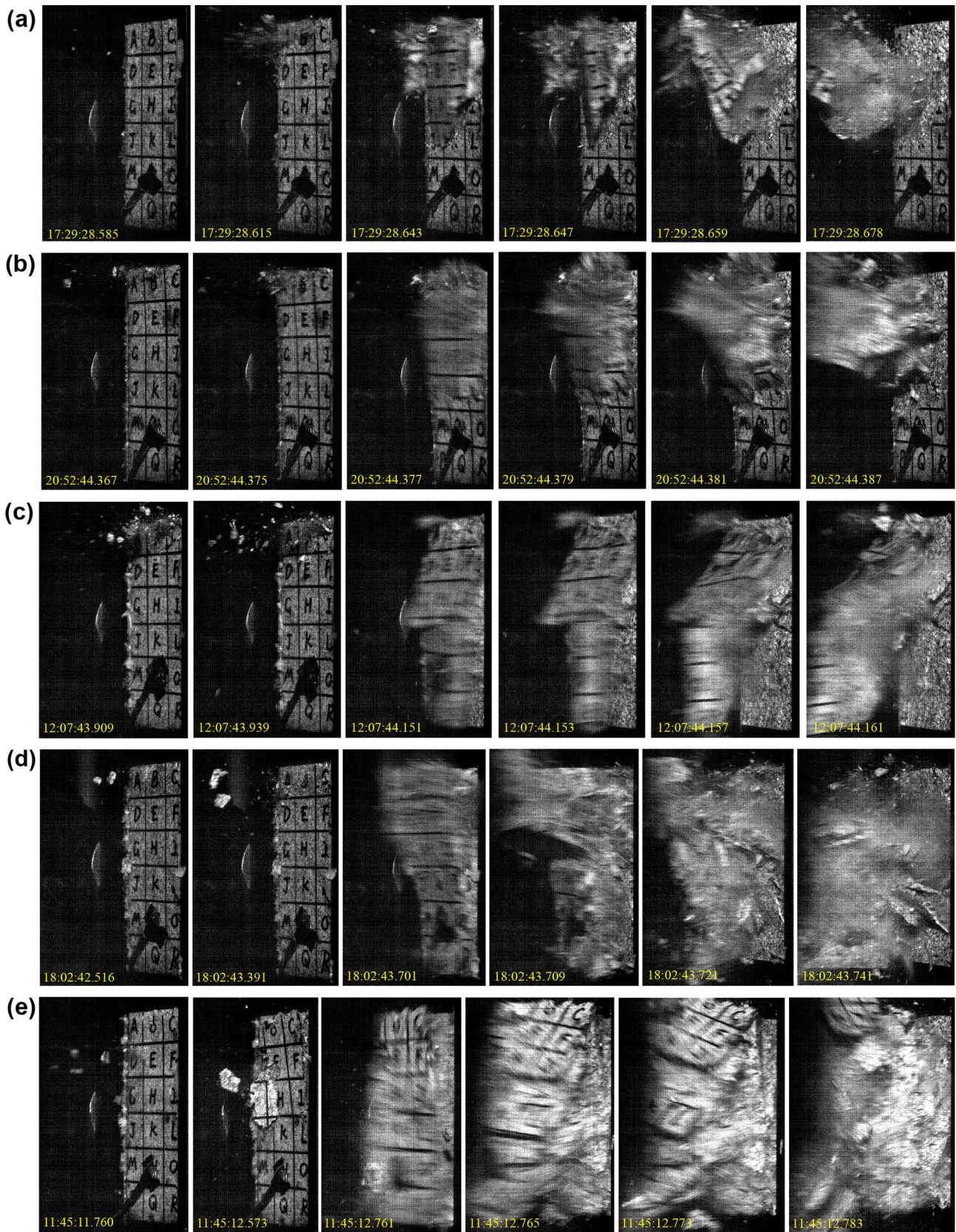


**Fig. 14** Failure processes of the lubricated specimens under different  $\sigma_2$  loading conditions: **a** 1 MPa, **b** 30 MPa, **c** 60 MPa, **d** 90 MPa, and **e** 120 MPa. The numbers at the bottom-left corner of the pictures indicate time in h:m:s

$\sigma_2$  is very low (e.g., 1 MPa), the end friction effect at the interfaces between the non-lubricated specimens and the platens is small. Therefore, the difference of the strainburst behaviors between the non-lubricated and lubricated specimens is not obvious. With increasing  $\sigma_2$ , the platen end effect strengthens. When splitting failure appears near the free surfaces of the specimens, the platen end friction generated from loading in  $\sigma_2$  direction limits the expansion of the specimen to the free surface and prevents the rock fragments from ejecting. Hence, when a non-lubricated specimen fails, a much stronger frictional constraint is exerted on the surfaces loaded by  $\sigma_2$ , resulting in less violent ejection of rock fragments. When the anti-friction agent is applied, the end friction constraint on specimen surfaces loaded by  $\sigma_2$  is reduced significantly. When a lubricated specimen fails, rock fragments are easier to be ejected out, leading to more violent failure and larger burst pits.

### 5.3 Influence of End Effect on Ejected Rock Fragment Characteristics

To investigate the influence of end effect on the mass of rock fragments ejected from the specimens under different  $\sigma_2$  conditions, the weights of the ejected fragments from each specimen were measured and the results are presented in Fig. 15. For the non-lubricated specimens, the fragment weight changes slightly when  $\sigma_2$  is less than 60 MPa. A rapid increase of the fragment weight occurs when  $\sigma_2$  ranges between 60 and 120 MPa. For the lubricated specimens, the fragment weight increases monotonically with the increase of  $\sigma_2$ , and the increase rate of the fragment weight increases as  $\sigma_2$  increases. This reflects that the specimens loaded with high  $\sigma_2$  values released more energy to trigger ejection of

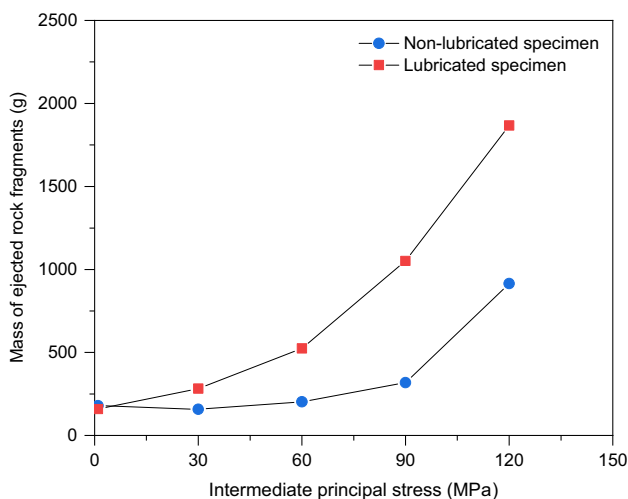


**Fig. 15** Influence of the end effect on mass of rock fragments ejected from the specimens under different  $\sigma_2$  loading conditions

the rock fragments than the specimens loaded with low  $\sigma_2$  values. When  $\sigma_2 = 1$  MPa, the data for the non-lubricated and lubricated specimens are very close to each other, indicating that the end effect has a negligible influence on the ejected fragment weight. However, under a  $\sigma_2$  higher than 1 MPa, the fragment weight of the lubricated specimen is larger than that of the non-lubricated specimen. This reveals that when the platen end friction effect is reduced effectively, fractured rock pieces are less constrained by the  $\sigma_2$  loading platens, resulting in larger weight of ejected rock fragments. In addition, with increasing  $\sigma_2$ , the platen end friction difference between the non-lubricated and lubricated specimens increases, leading to the increase of end constraint between them. Hence, the ejected fragment weight difference between the non-lubricated and lubricated specimens increases as  $\sigma_2$  increases.

To distinguish the size characteristics of the ejected rock fragments from the specimens after the test, the fragments were sieved into several groups using the standard sieves with different diameters. For example, the size distribution of the fragments for a lubricated specimen ( $\sigma_2 = 1$  MPa) is presented in Fig. 16. According to the fragment size ranges and the grain size classification system of igneous rocks (Strahle 2001), the fragments were further classified into five groups, i.e., large fragment (diameter  $d \geq 9.5$  mm), coarse fragment ( $4.75 \text{ mm} \leq d < 9.5$  mm), medium fragment ( $2.36 \text{ mm} \leq d < 4.75$  mm), fine fragment ( $0.3 \text{ mm} \leq d < 2.36$  mm), and micro fragment ( $d < 0.3$  mm) groups. The mass of each fragment group for each specimen was weighed, and subsequently its mass percentage was calculated and the results are presented in Fig. 17. It is seen that for all specimens, the mass percentage of the large fragment groups ranges from 67 to 94%, which is much larger than that of other fragment groups. The rock fragments in the large fragment groups are mainly thin plate-shaped, indicating the generation and ejection of extension fractures near the free surface of the specimens under compressive loading. For the non-lubricated and lubricated specimens, the mass percentage between the same fragment groups fluctuates and is not sensitive to  $\sigma_2$ , which means that  $\sigma_2$  has a little influence on the mass percentage of the fragment groups. In addition, under a constant  $\sigma_2$ , the mass percentage of the large fragment group of the lubricated specimen is larger than that of the non-lubricated specimen except for  $\sigma_2 = 1$  MPa, while the mass percentage of other fragment groups of the lubricated specimens is in general smaller than that of the non-lubricated specimens. This may reflect that under high  $\sigma_2$  loading conditions, the mass percentage of the large fragments ( $d \geq 9.5$  mm) ejected from the specimens can be improved when the end friction is reduced significantly.

**Fig. 16** Ejected rock fragments with different sizes (unit: mm) for the lubricated specimen under a  $\sigma_2$  of 1 MPa

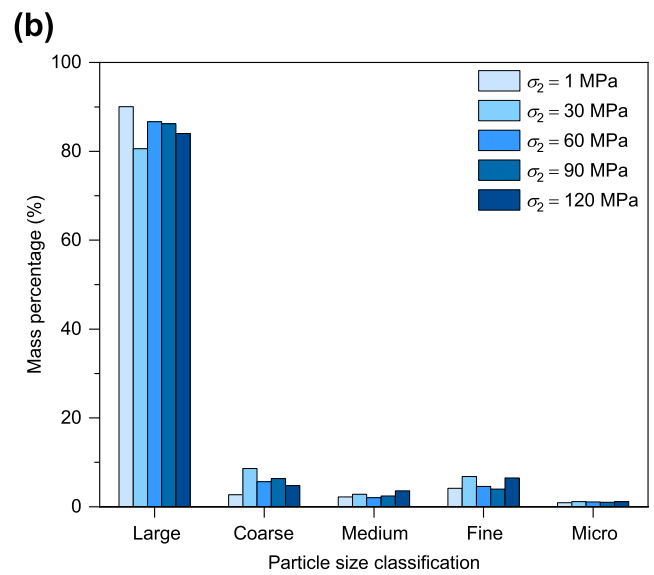
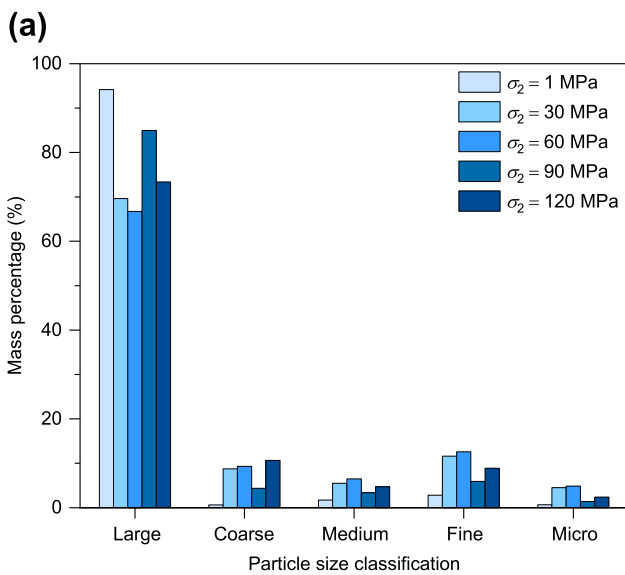
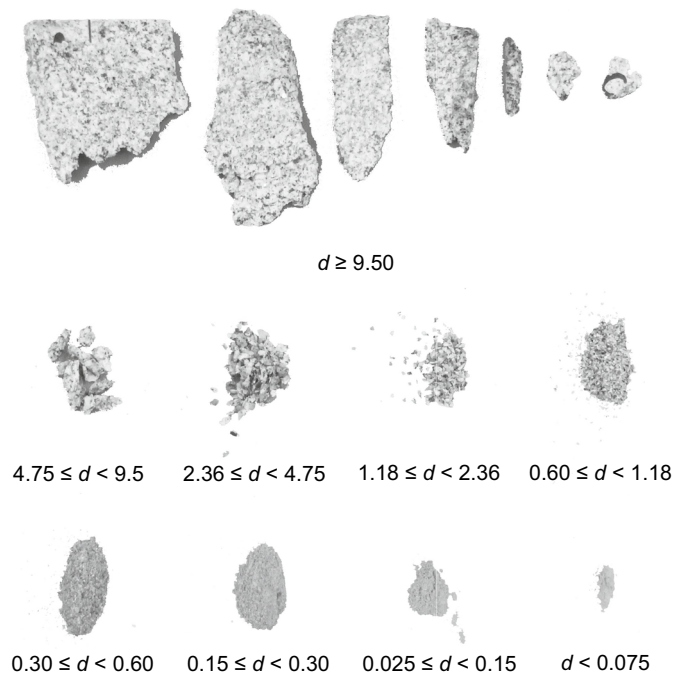


**Fig. 17** Mass percentage of the fragment groups classified from the ejected rock fragments from the specimens under different  $\sigma_2$  loading conditions. **a** Non-lubricated specimens and **b** lubricated specimens

### 5.4 Influence of End Effect on Kinetic Energy of Ejected Fragments

Rock damage is closely related to the energy released during failure of a rock. The kinetic energy of the ejected rock fragments is an important indicator to evaluate the strainburst damage intensity. The kinetic energy of an ejected rock fragment during a strainburst can be calculated by

$$E_k = \frac{1}{2}mv^2 \tag{1}$$

where  $m$  is the mass of the ejected rock fragment, and  $v$  is the speed of the fragment. In this work, the ejection speed of the rock fragments was measured through analyzing the fragment ejection videos recorded by the high-speed camera. To better track and distinguish the ejected fragments, the free surface of the specimens were divided into 18



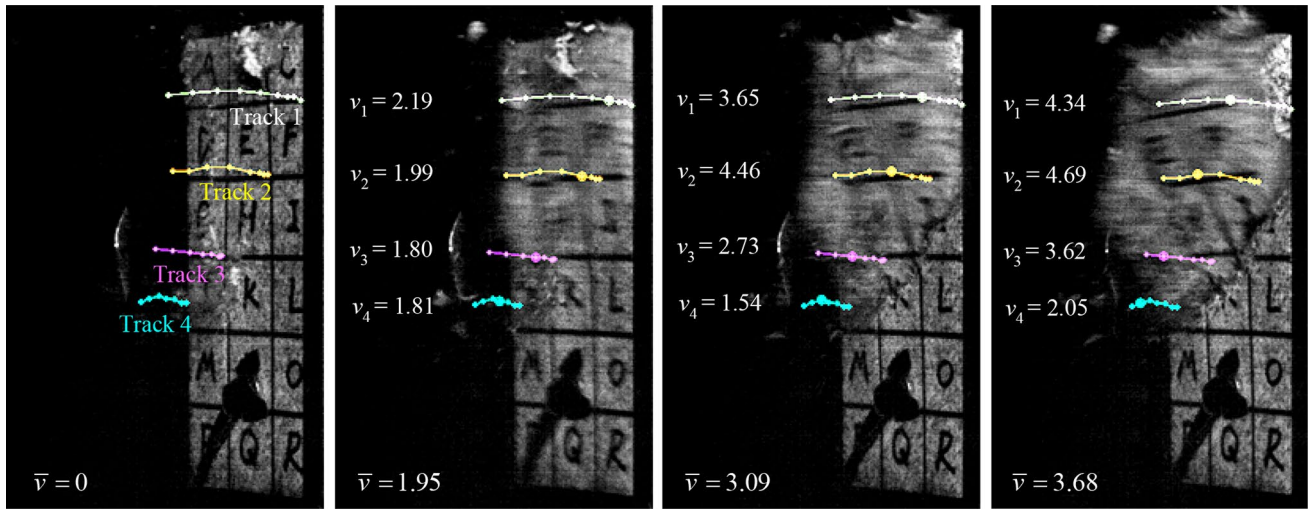


**Fig. 18** Schematic illustration of the speed measurement of rock fragments ejected from the non-lubricated specimen under a  $\sigma_2$  of 1 MPa using the dynamic image analysis software (unit: m/s)

sub-regions marked with different letters from A to R. A dynamic image analysis software (Image-Pro Plus 7.0) was used to capture the trajectories of the ejected fragments in the videos, and then the speed was calculated by dividing the distance along the trajectory by the corresponding time interval, as shown in Fig. 18.

Given that the ejection speed of small rock fragments ( $d < 4.75$  mm) was hard to be measured, only large and coarse fragment groups ( $d \geq 9.5$  mm and  $4.75$  mm  $\leq d < 9.5$  mm, as shown in Fig. 17) were used in our analysis. The large and coarse fragment groups contribute to the majority of the kinetic energy of ejected fragments for each specimen due to the dominant mass percentages of them (Fig. 17). For the large fragment group, the motion trail of each ejected fragment can be traced easily, and the ejection speed of each fragment is the average of speeds of several feature points on a fragment. For the coarse fragment group, the trajectory of each ejected fragment cannot be captured because many fragments are ejected in a relatively small region. Hence, the ejection speed of the coarse fragment group is the average speed of several representative fragments in a certain region. The total kinetic energy of the ejected fragments for a specimen can be expressed as

$$E_{kt} = \sum_{i=1}^n \frac{1}{2} m_{li} \bar{v}_{li}^2 + \frac{1}{2} M_c \bar{v}_c^2 \tag{2}$$

where  $n$  is the number of large fragments,  $m_{li}$  is the mass of  $i$ th large fragment,  $\bar{v}_{li}$  is the average speed of several points on the  $i$ th large fragment,  $M_c$  is the total mass of the coarse fragment group, and  $\bar{v}_c$  is the average speed of the coarse fragment group.

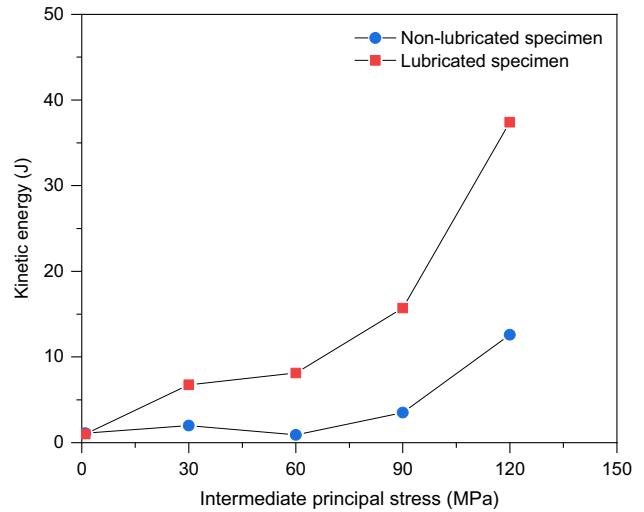


**Fig. 19** Kinetic energy of ejected rock fragments from the specimens under different  $\sigma_2$  loading conditions

Figure 19 shows the kinetic energy of ejected rock fragments from the specimens under different  $\sigma_2$  loading conditions. For the non-lubricated specimens under  $\sigma_2$  ranging from 1 to 60 MPa, the kinetic energy of the ejected fragments is relatively low and varies from 0.9 to 2.0 J. With  $\sigma_2$  increasing from 60 to 120 MPa, the kinetic energy of the ejected fragments increases rapidly up to 12.6 J and its increase rate increases, presenting high sensitivity to variations in  $\sigma_2$ . For the lubricated specimens, the kinetic energy of the ejected fragments increases remarkably as  $\sigma_2$  increases. At a given  $\sigma_2$  higher than 1 MPa, the kinetic energy of the ejected fragments from the lubricated specimen is much higher than that of the non-lubricated specimen, and the kinetic energy

difference between them increases with the increase of  $\sigma_2$ . For instance, when  $\sigma_2 = 120$  MPa, the kinetic energy of the ejected fragments from the lubricated specimen is approximately three times that of the non-lubricated specimen.

It is clear that for both non-lubricated and lubricated specimens, the kinetic energy of the ejected fragments presents an increasing trend with the increase of  $\sigma_2$ . When  $\sigma_2$  is small, less strain energy accumulates in the specimen and the loading system before failure. When a specimen fails, rock elements need to dissipate some strain energy when they deform into the free surface, resulting in less energy used for the ejection of rock fragments. Hence, the kinetic energy of the rock fragments is small. When  $\sigma_2$  is large, a large amount of strain energy is stored in the specimen and the loading system before failure. Once the strainburst is triggered, rock slabs and fragments are ejected at high speeds from the free surface in a very short period of time. In this case, the released strain energy cannot be dissipated in time and thus some energy is converted into kinetic energy of the rock fragments. On the other hand, when  $\sigma_2$  is high enough, the cracks are easy to initiate and propagate in the specimen (as discussed in Sect. 5.1), promoting the formation of rock slabs near the free surface of the specimen, and subsequently resulting in high intensity of the strainburst.

Similar to the response of mass of ejected rock fragments (Fig. 15), the end effect has a significant impact on the kinetic energy of rock fragments. When  $\sigma_2$  is small, the difference of the end effect at the specimen ends without and with anti-friction agent is small, which leads to a small difference of the dissipated energy during failure of the specimens. Accordingly, the difference of the kinetic energy of the rock fragments between the non-lubricated and lubricated specimens is small. As  $\sigma_2$  increases, the difference of the end effect between the non-lubricated and the lubricated specimens increases. When the specimens fail, the difference of the dissipated energy used for overcoming the end effect increases with increasing  $\sigma_2$ , resulting in the increase in the difference of the kinetic energy of the rock fragments between the non-lubricated and lubricated specimens.

## 6 Conclusions

The intermediate principal stress influences strongly the rock response near the excavation boundaries. A better understanding of  $\sigma_2$ -dependent mechanical behaviors of rocks at low confinements is important for safe underground construction. Although true-triaxial tests have been conducted by many researchers to simulate strainbursts in laboratory, few studies have addressed the influence of end effect at the specimen-platen contacts where  $\sigma_2$  is applied on strainbursts. In this work, rectangular prism specimens were tested under a special true-triaxial loading to investigate the influence of

end effect under loading in  $\sigma_2$  direction on the strainburst characteristics of Beishan granite. Based on the designed loading path, the strainburst tests on non-lubricated and lubricated specimens were performed successfully. The failure processes of the specimens under different  $\sigma_2$  loading conditions were captured by a high-speed camera. The crack initiation stresses and the peak strengths of the specimens were determined. The mass and size characteristics of rock fragments ejected from the specimens were also analyzed. Furthermore, the kinetic energy of ejected fragments was evaluated.

The experimental results indicated that whether the specimen ends are lubricated or not,  $\sigma_2$  has an impact on strainburst behaviors. The strainbursts are more violent for the specimens under higher  $\sigma_2$ . With increasing  $\sigma_2$ , the dynamic failure process of the specimens on the free surface shows a transition from local rock ejection to full-face burst. However, under a given  $\sigma_2$  ranging from 30 to 120 MPa, the degree of violence during the failure of the lubricated specimens is higher than that of the non-lubricated specimen. In addition, the end effect influences the crack initiation stress, the peak strength, failure mode, ejected rock fragment weight and associated kinetic energy of the rock. Under a given  $\sigma_2$ , the peak strength of the lubricated specimen is lower than that of the non-lubricated specimen, and the strength difference between them increases with the increase of  $\sigma_2$ . Moreover, compared with the lubricated specimens, the occurrence of the highest strength in the  $\sigma_1$ - $\sigma_2$  plot for the non-lubricated specimens is delayed. The crack initiation stress of the specimens is less dependent on  $\sigma_2$ . When the end effect is reduced, crack initiation can be induced at a lower stress level of  $\sigma_1$ , resulting in a lower peak strength of the specimen. It is also found that when the applied  $\sigma_2$  is sufficiently high, crack initiation of the specimens occurs during the process of applying  $\sigma_2$ . With increasing  $\sigma_2$ , the failure modes of the non-lubricated specimens change from splitting to shear, while the lubricated specimens mainly present splitting failure behavior. Under the same  $\sigma_2$ , the number of the fractures in the surfaces loaded by  $\sigma_2$  for the lubricated specimen is more than that for the non-lubricated specimen. Moreover, the weight and the kinetic energy of ejected rock fragments from the lubricated specimen are higher than those from the non-lubricated specimen. The difference of the weight and the kinetic energy of the rock fragments between the non-lubricated and lubricated specimens increases with the increase of  $\sigma_2$ .

In true-triaxial strainburst tests, results influenced by the end effect cannot represent real properties of rocks. Hence, when conducting true-triaxial tests to study strainburst characteristics of rocks under  $\sigma_2$  loading, attention should be paid to minimizing the end effect. It must be recognized that although the anti-friction agent was used in our tests, the end effect cannot be eliminated completely. More efforts

are needed to eliminate the end effect in laboratory tests to obtain results representative of field rock behaviors. In a future study, we plan to conduct true-triaxial tests for quantifying the influence of the end effect on strainbursts of Beishan granite using different anti-friction measures.

**Acknowledgements** This work has been supported by the China Atomic Energy Authority (CAEA) through the Geological Disposal Program and the National Natural Science Foundation of China (Grant No. 11972149). The authors would like to thank two anonymous reviewers and the associate editor (Prof. Arno Zang) for their valuable comments and suggestions. The excellent collaboration of all participants is highly appreciated.

#### Disclosures

**Conflict of interest** The authors declared that they have no conflicts of interest to this work.

## References

- Adoko AC, Gokceoglu C, Wu L, Zuo QJ (2013) Knowledge-based and data-driven fuzzy modeling for rockburst prediction. *Int J Rock Mech Min Sci* 61:86–95
- Al-Ajmi AM, Zimmerman RW (2005) Relation between the Mogi and the Coulomb failure criteria. *Int J Rock Mech Min Sci* 42:431–439
- Brace WF, Paulding BW, Scholz CH (1966) Dilatancy in the fracture of crystalline rocks. *J Geophys Res* 71:3939–3953
- Brady BT, Leighton FW (1977) Seismicity anomaly prior to a moderate rock burst: a case study. *Int J Rock Mech Min Sci Geomech Abst* 14:127–132
- Broch E, Sørheim S (1984) Experiences from the planning, construction and supporting of a road tunnel subjected to heavy rockbursting. *Rock Mech Rock Eng* 17:15–35
- Brown ET, Gonano LP (1974) Improved compression test technique for soft rock. *J Geotech Geoenviron Eng* 100:196–199
- Cai M (2008) Influence of intermediate principal stress on rock fracturing and strength near excavation boundaries—Insight from numerical modeling. *Int J Rock Mech Min Sci* 45:763–772
- Cai M (2009) A simple method to estimate tensile strength and Hoek-Brown strength parameter  $m_i$  of brittle rocks. In: Diederichs M, Grasselli G (eds.), *Proceedings of the 3rd CANUS Rock mechanics symposium*, Toronto, Paper 4063, 12p
- Cai M (2010) Practical estimates of tensile strength and Hoek-Brown strength parameter  $m_i$  of brittle rocks. *Rock Mech Rock Eng* 43:167–184
- Cai M (2013) Principles of rock support in burst-prone ground. *Tunn Undergr Space Technol* 36:46–56
- Cai M, Champaigne D (2012) Influence of bolt-grout bonding on MCB cone bolt performance. *Int J Rock Mech Min Sci* 49:165–175
- Cai M, Kaiser PK (2018) Rockburst support reference book—volume I: Rockburst phenomenon and support characteristics. [www.mirar.co.org](http://www.mirar.co.org)
- Chang C, Haimson B (2000) True triaxial strength and deformability of the German Continental Deep Drilling Program (KTB) deep hole amphibolite. *J Geophys Res* 105:18999–19013
- Chang C, Haimson B (2012) A failure criterion for rocks based on true triaxial testing. *Rock Mech Rock Eng* 45:1007–1010
- Cook NGW (1965) A note on rockburst considered as a problem of stability. *J S Afr Inst Min Metall* 65:437–446
- Cook NGW, Hoek E, Pretorius JPG, Ortlepp WD, Salamon MDG (1966) Rock mechanics applied to the study of rockbursts. *J S Afr Inst Min Metall* 66:435–528
- Diederichs MS (2007) The 2003 Canadian Geotechnical Colloquium: mechanistic interpretation and practical application of damage and spalling prediction criteria for deep tunnelling. *Can Geotech J* 44:1082–1116
- Eberhardt E, Stead D, Stimpson B (1999) Quantifying progressive pre-peak brittle fracture damage in rock during uniaxial compression. *Int J Rock Mech Min Sci* 36:361–380
- Fairhurst CE, Hudson JA (1999) Draft ISRM suggested method for the complete stress-strain curve for intact rock in uniaxial compression. *Int J Rock Mech Min Sci* 36:279–289
- Feng GL, Feng XT, Chen BR, Xiao YX (2015a) Microseismic sequences associated with rockbursts in the tunnels of the Jinping II hydropower station. *Int J Rock Mech Min Sci* 80:89–100
- Feng GL, Feng XT, Chen BR, Xiao YX, Yu Y (2015b) A microseismic method for dynamic warning of rockburst development processes in tunnels. *Rock Mech Rock Eng* 48:2061–2076
- Feng XT, Chen BR, Li SJ, Zhang CQ, Xiao YX, Feng GL, Zhou H, Qiu SL, Zhao ZN, Yu Y, Chen DF, Ming HJ (2012) Studies on the evolution process of rockbursts in deep tunnels. *J Rock Mech Geotech Eng* 4:289–295
- Feng XT, Haimson B, Li XC, Chang CD, Ma XD, Zhang XW, Ingraham M, Suzuki K (2019) ISRM suggested method: determining deformation and failure characteristics of rocks subjected to true triaxial compression. *Rock Mech Rock Eng* 52:2011–2020
- Feng XT, Kong R, Yang C, Zhang X, Wang Z, Han Q, Wang G (2020) A three-dimensional failure criterion for hard rocks under true triaxial compression. *Rock Mech Rock Eng* 53:25–29
- Feng XT, Liu JP, Chen BR, Xiao YX, Feng GL, Zhang FP (2017a) Monitoring, warning, and control of rockburst in deep metal mines. *Engineering* 3:538–545
- Feng XT, Zhang XW, Yang CX, Kong R, Liu XY, Peng S (2017b) Evaluation and reduction of the end friction effect in true triaxial tests on hard rocks. *Int J Rock Mech Min Sci* 97:144–148
- Feng XT, Zhang XW, Kong R, Wang G (2016) A novel Mogi type true triaxial testing apparatus and its use to obtain complete stress-strain curves of hard rocks. *Rock Mech Rock Eng* 49:1649–1662
- Gong QM, Yin LJ, Wu SY, Zhao J, Ting Y (2012) Rock burst and slabbing failure and its influence on TBM excavation at headrace tunnels in Jinping II hydropower station. *Eng Geol* 124:98–108
- Haimson B, Chang C (2000) A new true triaxial cell for testing mechanical properties of rock, and its use to determine rock strength and deformability of Westerly granite. *Int J Rock Mech Min Sci* 37:285–296
- He MC, Gong WL, Wang J, Qi P, Tao ZG, Du S, Peng YY (2014) Development of a novel energy-absorbing bolt with extraordinarily large elongation and constant resistance. *Int J Rock Mech Min Sci* 67:29–42
- He MC, Jia XN, Coli M, Livi E, Luís S (2012a) Experimental study of rockbursts in underground quarrying of Carrara marble. *Int J Rock Mech Min Sci* 52:1–8
- He MC, Miao JL, Feng JL (2010) Rock burst process of limestone and its acoustic emission characteristics under true-triaxial unloading conditions. *Int J Rock Mech Min Sci* 47:286–298
- He MC, Miao JL, Li DJ (2007) Experimental study on rockburst processes of granite specimen at great depth. *Chin J Rock Mechan Eng* 26:865–876 (**in Chinese**)
- He MC, Nie W, Zhao ZY, Guo W (2012b) Experimental Investigation of bedding plane orientation on the rockburst behavior of sandstone. *Rock Mech Rock Eng* 45:311–326

- He MC, e Sousa LR, Miranda T, Zhu GL (2015) Rockburst laboratory tests database — Application of data mining techniques. *Eng Geol* 185:116–130
- Hedley DGF (1992) Rockburst handbook for Ontario hardrock mines, CANMET Special Report SP92-1E
- ISRM (1978) Suggested methods for determining tensile strength of rock materials. *Int J Rock Mech Min Sci Geomech Abstr* 15:99–103
- ISRM (1979) Suggested methods for determining water content, porosity, density, absorption and related properties and swelling and slake-durability index properties. *Int J Rock Mech Min Sci Geomech Abstr* 16:143–151
- Jiang Q, Su GS, Feng XT, Cui J, Pan PZ, Jiang JQ (2015) Observation of rock fragment ejection in post-failure response. *Int J Rock Mech Min Sci* 74:30–37
- Kaiser PK (2009) Seismic hazard evaluation in underground construction. In: *Proceedings of Seventh International Symposium on Rock burst and Seismicity in Mines*, Dalian, pp 1–26
- Kaiser PK, Cai M (2012) Design of rock support system under rockburst condition. *J Rock Mech Geotech Eng* 4:215–227
- Kaiser PK, Diederichs MS, Martin CD, Sharp J, Steiner W (2000) Underground works in hard rock tunnelling and mining. Keynote lecture at GeoEng2000. Technomic Publishing Co, Melbourne, pp 841–926
- Kaiser PK, McCreath DR, Tannant DD (1996) Canadian rockburst support handbook. CAMIRO, Sudbury
- Konicek P, Ptacek J, Waclawik P, Kajzar V (2018) Long-term Czech experiences with rockbursts with applicability to today's underground coal mines. *Rock Mech Rock Eng* 52:1447–1458
- Kwasniewski M, Takahashi M, Li X (2003) Volume changes in sandstone under true triaxial compression conditions, ISRM 2003 - Technology roadmap for rock mechanics. South African Institute of Mining and Metallurg, pp 683–688
- Labuz JF, Bridell JM (1993) Reducing frictional constraint in compression testing through lubrication. *Int J Rock Mech Min Sci Geomech Abstr* 30:451–455
- Lajtai EZ (1974) Brittle fracture in compression. *Int J FractMech* 10:525–536
- Lee H, Haimson BC (2011) True triaxial strength, deformability, and brittle failure of granodiorite from the San Andreas Fault Observatory at Depth. *Int J Rock Mech Min Sci* 48:1199–1207
- Leveille P, Sepelri M, Apel DB (2017) Rockbursting potential of kimberlite: a case study of Diavik diamond mine. *Rock Mech Rock Eng* 50:3223–3231
- Li CC (2010) A new energy-absorbing bolt for rock support in high stress rock masses. *Int J Rock Mech Min Sci* 47:396–404
- Li SJ, Feng XT, Li ZH, Chen BR, Zhang CQ, Zhou H (2012) In situ monitoring of rockburst nucleation and evolution in the deeply buried tunnels of Jinping II hydropower station. *Eng Geol* 137–138:85–96
- Li XB, Du K, Li DY (2015) True triaxial strength and failure modes of cubic rock specimens with unloading the minor principal stress. *Rock Mech Rock Eng* 48:2185–2196
- Li XB, Feng F, Li DY, Du K, Ranjith PG, Rostami J (2018) Failure characteristics of granite influenced by sample height-to-width ratios and intermediate principal stress under true-triaxial unloading conditions. *Rock Mech Rock Eng* 51:1321–1345
- Linkov AM (1996) Rockbursts and the instability of rock masses. *Int J Rock Mech Min Sci Geomech Abstr* 33:727–732
- Ma TH, Tang CA, Tang LX, Zhang WD, Wang L (2015) Rockburst characteristics and microseismic monitoring of deep-buried tunnels for Jinping II Hydropower Station. *Tunn Undergr Space Technol* 49:345–368
- Manouchehrian A, Cai M (2016) Simulation of unstable rock failure under unloading conditions. *Can Geotech J* 53:22–34
- Manouchehrian A, Cai M (2018) Numerical modeling of rockburst near fault zones in deep tunnels. *Tunn Undergr Space Technol* 80:164–180
- Martin CD, Chandler NA (1994) The progressive fracture of Lac du Bonnet granite. *Int J Rock Mech Min Sci Geomech Abstr* 31:643–659
- Miao SJ, Cai MF, Q.F. Guo, Huang ZJ, (2016) Rock burst prediction based on in-situ stress and energy accumulation theory. *Int J Rock Mech Min Sci* 83:86–94
- Mogi K (1971) Fracture and flow of rocks under high triaxial compression. *J Geophys Res* 76:1255–1269
- Mogi K (1972) Effect of the triaxial stress system on fracture and flow of rocks. *Phys Earth Planetary* 5:318–324
- Mogi K (1977) Dilatancy of rocks under general triaxial stress states with special reference to earthquake precursors. *J Phys Earth* 25:203–217
- Mogi K (2007) *Experimental rock mechanics*. CRC Press, London
- Nicksiar M, Martin CD (2012) Evaluation of methods for determining crack initiation in compression tests on low-porosity rocks. *Rock Mech Rock Eng* 45:607–617
- Ortlepp WD, Stacey TR (1994) Rockburst mechanisms in tunnels and shafts. *Tunn Undergr Space Technol* 9:59–65
- Pan PZ, Feng XT, Hudson JA (2012) The influence of the intermediate principal stress on rock failure behaviour: a numerical study. *Eng Geol* 124:109–118
- Pellegrino A, Sulem J, Barla G (1997) The effects of slenderness and lubrication on the uniaxial behavior of a soft limestone. *Int J Rock Mech Min Sci* 34:333–340
- Salamon MDG (1970) Stability, instability, and design of pillar workings. *Int J Rock Mech Min Sci Geomech Abstr* 7:613–631
- Singh SP (1987) The influence of rock properties on the occurrence and control of rockbursts. *Min Sci Technol* 5:11–18
- Srinivasan C, Arora SK, Benady S (1999) Precursory monitoring of impending rockbursts in Kolar gold mines from microseismic emissions at deeper levels. *Int J Rock Mech Min Sci* 36:941–948
- Stacey TR (1981) A simple extension strain criterion for fracture of brittle rock. *Int J Rock Mech Min Sci Geomech Abstr* 18:469–474
- Stacey TR (2016) Addressing the consequences of dynamic rock failure in underground excavations. *Rock Mech Rock Eng* 49:4091–4101
- Strahle A (2001) Definition och beskrivning av parametrar för geologisk, geofysisk och bergmekanisk kartering av berg: R-01–19.
- Su GS, Hu LH, Feng XT, Yan LB, Zhang GL, Yan SZ, Zhao B, Yan ZF (2018) True triaxial experimental study of rockbursts induced by ramp and cyclic dynamic disturbances. *Rock Mech Rock Eng* 51:1027–1045
- Su GS, Chen ZY, Ju JW, Jiang JQ (2017a) Influence of temperature on the strainburst characteristics of granite under true triaxial loading conditions. *Eng Geol* 222:38–52
- Su GS, Feng XT, Wang JH, Jiang JQ, Hu LH (2017b) Experimental study of remotely triggered rockburst induced by a tunnel axial dynamic disturbance under true-triaxial conditions. *Rock Mech Rock Eng* 50:2207–2226
- Su GS, Jiang JQ, Zhai SB, Zhang GL (2017c) Influence of tunnel axis stress on strainburst: an experimental study. *Rock Mech Rock Eng* 50:1551–1567
- Su GS, Zhai SB, Jiang JQ, Zhang GL, Yan LB (2017d) Influence of radial stress gradient on strainbursts: an experimental study. *Rock Mech Rock Eng* 50:2659–2676
- Su GS, Jiang JQ, Feng XT, Mo C, Jiang Q (2016) Experimental study of ejection process in rockburst. *Chin J Rock Mechan Eng* 35:1990–1999 (**In Chinese**)
- Takahashi M, Koide H (1989) Effect of the intermediate principal stress on strength and deformation behavior of sedimentary rocks at the depth shallower than 2000 m. In: Z Ma and DG Seiler (eds.),

- International Symposium on Rock at Great Depth. Balkema, pp 19–26
- Wang CL, Wu AX, Lu H, Bao TC, Liu XH (2015) Predicting rockburst tendency based on fuzzy matter–element model. *Int J Rock Mech Min Sci* 75:224–232
- Wang J-A, Park HD (2001) Comprehensive prediction of rockburst based on analysis of strain energy in rocks. *Tunn Undergr Space Technol* 16:49–57
- Wang J, Chen L, Su R, Zhao XG (2018) The Beishan underground research laboratory for geological disposal of high-level radioactive waste in China: planning, site selection, site characterization and in situ tests. *J Rock Mech Geotech Eng* 10:411–435
- Wiebols G, Cook N (1968) An energy criterion for the strength of rock in polyaxial compression. *Int J Rock Mech Min Sci Geomech Abst* 5:529–549
- Xu NW, Li TB, Dai F, Zhang R, Tang CA, Tang LX (2016) Microseismic monitoring of strainburst activities in deep tunnels at the Jinping II Hydropower Station, China. *Rock Mech Rock Eng* 49:981–1000
- Xu YH, Cai M, Feng XT, Zhang XW, Li YH (2020) A method to remove end effect for the determination of intrinsic 3D rock strength envelopes. *Int J Rock Mech Min Sci* 131:28–29
- Xu YH, Cai M, Zhang XW, Feng XT (2017) Influence of end effect on rock strength in true triaxial compression test. *Can Geotech J* 54:862–880
- You MQ (2009) True-triaxial strength criteria for rock. *Int J Rock Mech Min Sci* 46:115–127
- Yu MH, Zan YW, Zhao J, Yoshimine M (2002) A unified strength criterion for rock material. *Int J Rock Mech Min Sci* 39:975–989
- Yun XY, Mitri HS, Yang XL, Wang YK (2010) Experimental investigation into biaxial compressive strength of granite. *Int J Rock Mech Min Sci* 47:334–341
- Zhang CQ, Feng XT, Zhou H, Qiu SL, Wu WP (2012) Case histories of four extremely intense rockbursts in deep tunnels. *Rock Mech Rock Eng* 45:275–288
- Zhao XG, Cai M (2015) Influence of specimen height-to-width ratio on the strainburst characteristics of Tianhu granite under true-triaxial unloading conditions. *Can Geotech J* 52:890–902
- Zhao XG, Cai M, Wang J, Li PF (2015a) Strength comparison between cylindrical and prism specimens of Beishan granite under uniaxial compression. *Int J Rock Mech Min Sci* 76:10–17
- Zhao XG, Cai M, Wang J, Li PF, Ma LK (2015b) Objective determination of crack initiation stress of brittle rocks under compression using AE measurement. *Rock Mech Rock Eng* 48:2473–2484
- Zhao XG, Wang J, Ma LK, Cai M, Li PF (2015c) A new approach to identify crack initiation stress of crystalline rocks under uniaxial compression condition, ISRM 2015, Montreal, Paper 221, 9p
- Zhao XG, Cai M, Wang J, Ma LK (2013) Damage stress and acoustic emission characteristics of the Beishan granite. *Int J Rock Mech Min Sci* 64:258–269
- Zhao XG, Wang J, Cai M, Cheng C, Ma LK, Su R, Zhao F, Li DJ (2014) Influence of unloading rate on the strainburst characteristics of Beishan granite under true-triaxial unloading conditions. *Rock Mech Rock Eng* 47:467–483
- Zhu WC, Li ZH, Zhu L, Tang CA (2010) Numerical simulation on rockburst of underground opening triggered by dynamic disturbance. *Tunn Undergr Space Technol* 25:587–599

**Publisher's Note** Springer Nature remains neutral with regard to jurisdictional claims in published maps and institutional affiliations.